

POLITECNICO DI TORINO

MASTER'S DEGREE IN ELECTRICAL ENGINEERING

A.Y. 2023/2024

Thesis Title:

**Analysis and Simulation of a
Bidirectional CLLC Resonant Converter**



**Politecnico
di Torino**

Supervisor

Iustin Radu BOJOI

Co-Supervisor

Alessandro BADOGLIO

Candidate

Rebecca GIOCO

March 2024

Ai miei angeli
Mamma, Nonna e Enzo

Abstract

Carbon Neutrality by 2050 is the goal of the European Green Deal. From the Smart Grids point of view, in which BEVs (Battery Electrical Vehicles) participate in the stabilization of the network through the V2G (vehicle-to-grid) configuration, the development and the installation of bidirectional chargers therefore becomes a necessity.

The state of the art sees the emerging birth of CLLC resonant converters, characterized by greater efficiency compared to previous bidirectional DAB (Dual Active Bridge) and unidirectional LLC resonant converters.

The research and development work conducted at the company Prima Electro had the objective of using the results obtained as a first evaluation tool for the possible creation of CLLC resonant converters.

Using the FHA (First-Harmonic-Approximation) concept known from the literature, an analytical study has been conducted on a converter simplified model to obtain the formulas describing its frequency behaviour. The expression of the voltage gain depending on the operating frequency and defining the buck or boost operation mode has been obtained first. Then, the inductive and capacitive behaviour was studied as a function of frequency to ensure Soft Switching operation. To conclude the analytical procedures the expression of the delay for controlling the rectifier bridge switches was found to guarantee the SR (Synchronous Rectification) and to limit the losses.

Finally, simulations were conducted on PLECS to verify the validity of the analytical models, to evaluate the error made with the assumptions, and as a tool to map the operating regions of the converter. Furthermore, component stresses were evaluated, as an evaluation tool for future design work.

Contents

1	Introduction	1
1.1	Motivation	1
1.2	Thesis Objectives	4
1.3	Personal Contributions	4
2	CLLC General Technical Aspects	7
2.1	Charging Systems General Aspect	7
2.2	CLLC Resonant Converter	9
2.2.1	Types of CLLC Resonant Converter	9
2.2.2	Synchronous Rectification	12
3	Theoretical Analysis and Model	15
3.1	Equivalent Circuit with FHA	15
3.2	Gain Analysis	20
3.3	ZVS Region Boundary	22
3.4	Phase Shift Estimation	25
4	Plecs Simulations Results	29
4.1	Equivalent Output Resistance Model	29
4.2	Sinusoidal Model	32
4.2.1	Sinusoidal Model Validation	33
4.2.2	Sinusoidal Model Working Points Map	34
4.3	Square Wave Model	38
4.3.1	Square Wave Model Validation	39
4.3.2	Square Wave Model Working Points Map	41
4.4	Inverting and Rectifying Bridge Model	43
4.4.1	Inverting and Rectifying Bridge Model Validation	44
4.4.2	Inverting and Rectifying Bridge Model Working Points Map	46
4.5	CLLC Resonant Converter Circuit	48
4.5.1	CLLC circuit Validation	48

4.5.2	CLLC circuit Working Points Map	50
5	Stresses Evaluation	53
5.0.1	Primary Side Resonant Inductor Stresses	53
5.0.2	Secondary Side Resonant Inductor Stresses	56
5.0.3	Transformer Stresses	59
5.0.4	Primary Side Resonant Capacitor Stresses	62
5.0.5	Primary Side Resonant Capacitor Stresses	63
5.0.6	MOSFETs Current Stresses	64
6	Conclusions and Future Works	67
6.1	Conclusions	67
6.2	Future Works	68
A	Calculation Gain Formula in Forward Mode	69
B	Calculation Gain Formula in Reverse Mode	73
C	Calculation of the Input Impedance	77

List of Figures

1.1	Energy trilemma [1]	1
1.2	Smart grid configuration [3].	2
1.3	Regional Trends in Public Light-Duty Vehicle Charger Installations (2022-2030)[5].	3
2.1	Conductive chargers: (a) On-board chargers; (b) Off-board chargers [6].	7
2.2	Wireless charging [7].	8
2.3	Battery swapping [8].	8
2.4	Configuration of the four CLLC resonant converters types.	10
2.5	Bidirectional CLLC resonant converters: (a) Symmetrical Full Bridge CLLC; (b) Asymmetrical Full Bridge CLLC; (c) Symmetrical Half Bridge CLLC; (d) Asymmetrical Half Bridge CLLC.	11
2.6	Equivalent output resistance.	12
2.7	Switch command signals.	13
2.8	SR methods for CLLC converter: (a) theoretical calculation, (b) voltage sensing and (c) current sensing [12].	14
3.1	Voltages of: (a) Full bridge converter; (b) Half bridge converter.	16
3.2	Equivalent circuits : (a) Equivalent circuit of SFBCLLC; (b) Equivalent circuit of AFBCLLC; (c) Equivalent circuit of SHBCLLC ; (d) Equivalent circuit of AHBCLLC.	17
3.3	Unified equivalent circuit in forward mode.	19
3.4	Unified equivalent circuit in reverse mode.	19
3.5	Transfer function of CLLC.	21
3.6	Inductive limit for ZVS operation.	23
3.7	Operation in the inductive region.	24
3.8	Operation in the capacitive region.	25
3.9	Phase shift from theoretical calculations.	26
3.10	CLLC equivalent circuit modeled on LTspice.	26
3.11	Phase shift from LTspice.	27

LIST OF FIGURES

4.1	Equivalent resistance model.	30
4.2	Diagram of the phase shift calculation.	30
4.3	”Phase shift integrator” block.	31
4.4	Comparison between calculated and obtained phase.	31
4.5	Error between theoretical and obtained phase shift.	32
4.6	Sinusoidal model.	33
4.7	Calculation of equivalent output resistance in the sinusoidal model.	34
4.8	Comparison of voltage gain between the theoretical model and the obtained results in the sinusoidal model.	36
4.9	Output current map in the sinusoidal model.	37
4.10	Output power map in the sinusoidal model.	38
4.11	Square wave model.	39
4.12	Calculation of equivalent output resistance in square wave model.	40
4.13	Comparison between the imposed and obtained equivalent output resistance in square wave model.	40
4.14	Relative percentage error between the imposed and obtained equivalent output resistance in square wave model.	41
4.15	Comparison of voltage gain between the theoretical model and the obtained results in the square wave model.	42
4.16	Output current map in the sinusoidal model.	42
4.17	Output power map in the sinusoidal model.	43
4.18	Inverting and rectifying bridge model.	44
4.19	Calculation of equivalent output resistance in inverting and rectifying bridge model.	44
4.20	Comparison between the imposed and obtained equivalent output resistance in inverting and rectifying bridge model.	45
4.21	Relative percentage error between the imposed and obtained equivalent output resistance in inverting and rectifying bridge model.	45
4.22	47
4.23	CLLC resonant converter schematic.	48
4.24	Calculation of equivalent output resistance in CLLC resonant converter schematic.	48
4.25	(a) comparison between imposed and obtained equivalent output resistance in CLLC scheme; (b) relative percentage error between the imposed and obtained equivalent output resistance in CLLC scheme.	49
4.26	Comparison of voltage gain between the theoretical model and the obtained results in CLLC scheme.	50
4.27	Output current map in in CLLC scheme.	51
4.28	Output power map in CLLC scheme.	51

LIST OF FIGURES

5.1	RMS current of primary resonant inductor.	54
5.2	Peak current of primary resonant inductor.	54
5.3	Peak voltage of primary resonant inductor.	55
5.4	Maximum flux of primary resonant inductor.	56
5.5	RMS current of secondary resonant inductor.	57
5.6	Peak current of secondary resonant inductor.	58
5.7	Peak voltage of secondary resonant inductor.	58
5.8	Maximum flux of secondary resonant inductor.	59
5.9	RMS current of transformer.	60
5.10	Peak current of transformer.	60
5.11	Peak voltage of transformer.	61
5.12	Maximum flux of transformer.	62
5.13	Peak voltage of primary side capacitor.	63
5.14	Peak voltage of secondary side capacitor.	64
5.15	MOSFET 1 RMS current.	65
5.16	MOSFET 1 peak current.	65
5.17	MOSFET 5 RMS current.	66
5.18	MOSFET 5 peak current.	66
A.1	Equivalent circuit of SFBCLLC in forward mode.	70
B.1	Equivalent circuit of in reverse mode.	73

LIST OF FIGURES

List of Tables

3.1	Calculation of phase shift.	26
4.1	Parameters of CLLC.	29
5.1	Quantities of interest for sizing.	53

LIST OF TABLES

Chapter 1

Introduction

1.1 Motivation

Nowadays, the electricity system feels the need to start an energy transition due to the impacts that energy use has on a three-dimensional framework called "Energy trilemma" shown in Fig.1.1. This concept outlines the need to achieve a balance between energy reliability, affordability, and sustainability.

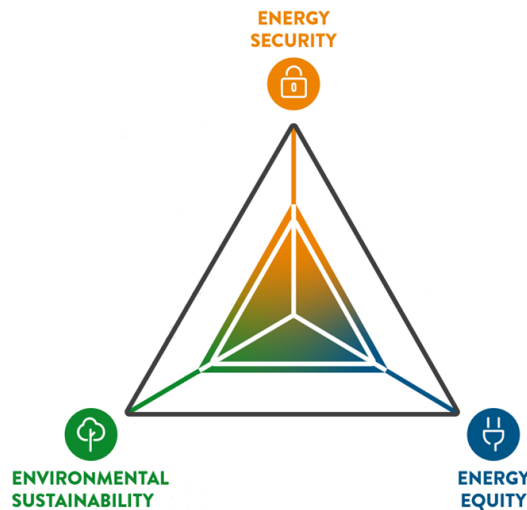


Figure 1.1: Energy trilemma [1]

Firstly, the actual energy use has impacts on the environment compromising the basic needs of human life like the air, water, and food quality. At a global and European level, the need to move towards a sustainable production system has arisen. The European Green Deal aims for climate neutrality by 2050 and a 32% emissions reduction by

2030. Globally, initiatives such as the Paris Agreement and Mission Innovation promote innovation and collaboration in clean energy. These efforts emphasize renewable energy, efficient technologies, and interconnected grids for a sustainable future. Furthermore, the European Roadmap to 2050 indicates some targets with a common point: “The share of renewables rises substantially in all scenarios, achieving at least 55% in gross final energy consumption in 2050”, which requires “smart infrastructure including electrical storage“ [2].

Secondly, society and economics characterize the equity dimension. This concept embraces the economic prosperity of a nation measured by its purchasing power, but is also closely tied to the mental and physical well-being of its inhabitants.

Lastly, there’s the dimension of security, which encompasses geopolitical conflicts and the reliability of the electricity grid. Although seemingly disparate, these two are interconnected. Geopolitical conflicts often create problems that compromise the reliability and accessibility of the electricity system, see the hostilities between Russia and Ukraine.



Figure 1.2: Smart grid configuration [3].

A race towards smart grids is underway to improve the stability of the electricity system. From this perspective, the production-transmission and distribution system passes from a centralized to a distributed system, from a vertical to a horizontal structure. This type of system sees the active participation of the final users who become “prosumers” to indicate that they are both producers and users of electricity. A representation of the main characteristics of smart grids is shown in Fig.1.2.

In this scenario, one of the active roles of the prosumers is to participate in the storage system through the V2G configuration. The Vehicle-to-Grid (V2G) technology facilitates electric vehicles to discharge during grid power insufficiency and charge during

1.1. MOTIVATION

excess power availability through incentives like electricity pricing. V2G offers flexible and cost-effective energy storage for the grid while presenting a new solution for integrating renewable energy and optimizing power grid operations. Additionally, it allows electric vehicle owners to benefit from incentive policies and utilize their vehicles as idle resources [4].

In this concept, the charging infrastructure for Electric Vehicles (EVs) is poised to be a crucial factor in decarbonization over the coming decades. This will enhance the pivotal role of power electronics converters as a key technology in the broad acceptance of clean energy sources and their efficient utilization during the energy transition.

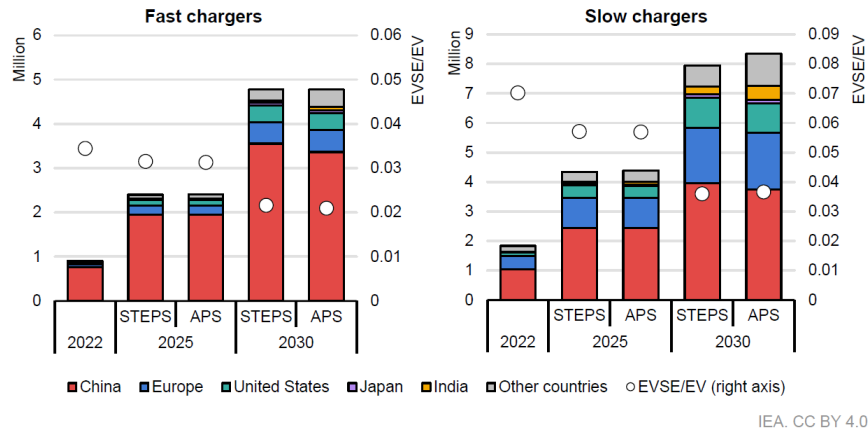


Figure 1.3: Regional Trends in Public Light-Duty Vehicle Charger Installations (2022-2030)[5].

According to IEA estimates [5], the total number of public chargers needed to support LDV (light electric vehicles) electrification in the world by 2030 is projected in Fig.1.3. The principal contribution will come from China with an estimation of 7.5 million public charging stations, while in Europe, the stock of public chargers is expected to increase to around 2.4 million.

An important role in the charging infrastructure is played by the DC transformer (DCX), which retains all the functionality of a traditional transformer, but unlike this one, the frequencies involved are much higher resulting in benefits such as smaller dimensions, less weight, rapid response, and low impedance.

1.2 Thesis Objectives

The main objective of the present work is the development of a research work thesis on the CLLC bidirectional resonant converter conducted at Prima Electro company (Moncalieri, TO) in order to give a first evaluation tool for the possible creation of this kind of converter. The company is actively involved in the converter market and is particularly interested in the high power density and efficiency offered by these converters, hence providing an opportunity to undertake this research thesis.

The specific objective is therefore to conduct analytical and theoretical studies on the operation of the converter and on its frequency behavior. This groundwork will lay the foundation for the second step, which involves using simulation tools to evaluate component stresses at various operating points, using an existing converter as a model. This tool will be valuable in the post-design process, although it's not the focus of this thesis. It will help determine the appropriate size for components based on the stresses identified through this tool.

1.3 Personal Contributions

Firstly, an extensive literature search was conducted to study the CLLC resonant converter. Theory imposes the necessity of deriving a simplified model to study the circuit, operating under the assumption that this simplified model accurately represents the behaviour of the complex circuit.

The simplified model was derived starting from the FHA assumption, enabling the analysis of the circuit under sinusoidal conditions and the application of established methods from electrotechnics. This approach assigns all the energy contribution from the conversion only to the fundamental harmonic. When dealing with a circuit under sinusoidal supply, a transition to phasor analysis can be made to study the circuit behaviour in the frequency domain.

The expression of the voltage gain was derived from the simplified model, representing a transfer function between the output and input. This expression indicates whether the converter operates in buck (step-down) or boost (step-up) mode depending on the operating frequency and the load's absorption.

Subsequently, the inductive and capacitive behaviour of the converter was studied to ensure Soft Switching operation by examining the sign of the imaginary part of the impedance at the input terminals. Therefore, the frequency spectrum that guarantees

1.3. *PERSONAL CONTRIBUTIONS*

the inductive behaviour was identified.

To conclude the analytical procedures, a mathematical method was proposed for calculating the phase shift expression used to control the rectifier bridge in order to ensure Synchronous Rectification and limit the losses.

Furthermore, simulations were performed on an existing converter in the PLECS simulation environment to validate the analytical model. The simulations were conducted reversely compared to the analytical steps, starting from the simplified circuit and progressing toward the resonant CLLC converter model. Qualitative and quantitative evaluations were conducted from these simulations to assess the error incurred from the assumptions made. Additionally, maps of the operating regions of the converter were extrapolated.

Finally, stress maps for the components were derived from the PLECS simulation, intending to provide a useful tool for component sizing in the post-design phase, in order to evaluate the necessary conductor insulation, conductor section, and magnetic core section, topics not evaluated in this thesis work.

CHAPTER 1. INTRODUCTION

Chapter 2

CLLC General Technical Aspects

2.1 Charging Systems General Aspect

Power electronic systems utilized in EV charging must address various simultaneous requirements like safe battery charging, compliance with grid harmonic standards, efficiency, compactness, and reliability.

The power electronics configuration of a typical EV supply equipment (EVSE) is structured as a two-stage system: a rectifier stage with power-factor correction (PFC) connected to AC mains, which may vary from single phase to three phases based on the power requirements; a DC–DC stage responsible for regulating battery voltage and current.

Charging methods are categorized into conductive chargers, wireless chargers, and battery swapping. In the category of conductive chargers, there are On-board Chargers (OBC) and Off-board chargers.

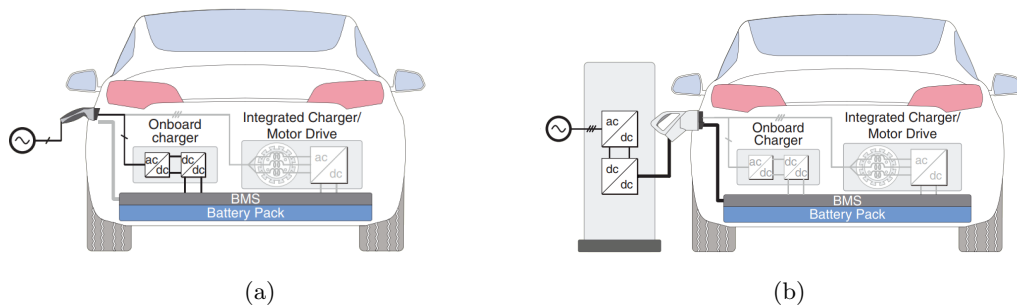


Figure 2.1: Conductive chargers: (a) On-board chargers; (b) Off-board chargers [6].

On-board Chargers (OBC) are powered by dedicated AC charging stations or domestic outlets (wall box) with capacities of 3.3 kW or 22 kW, as shown in Fig.2.1a. The conversion stages from AC/DC and DC/DC are all done on board of the vehicle and Off-board chargers. OBCs must seamlessly connect to outlets worldwide, facing challenges due to varying AC voltage magnitudes and frequencies globally.

On the other hand, Off-board DC chargers, shown in Fig.2.1b, differ fundamentally from AC charging solutions as the vehicle exposes its battery to the outside and most power conversion occurs externally. This external conversion allows for charging powers that can exceed 50 kW without the need for massive on-board electronics.

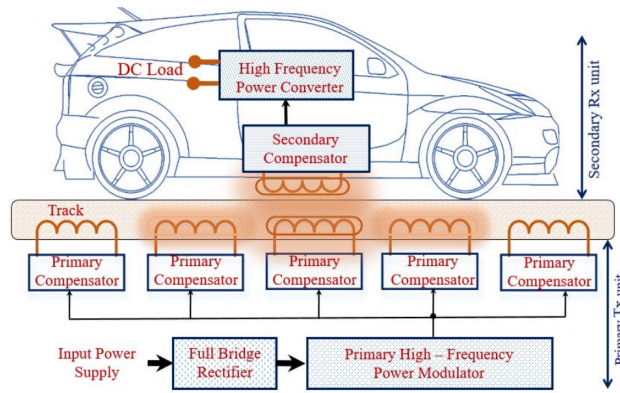


Figure 2.2: Wireless charging [7].

In Fig.2.2 the wireless resonant inductive power transfer (WRIPT) charger system is shown. It uses the magnetic resonance inductive coupling principle and consists of a primary wireless source power transmitting unit coupled with a secondary receiving device [7]. However, these technologies are still in the research and development phase.

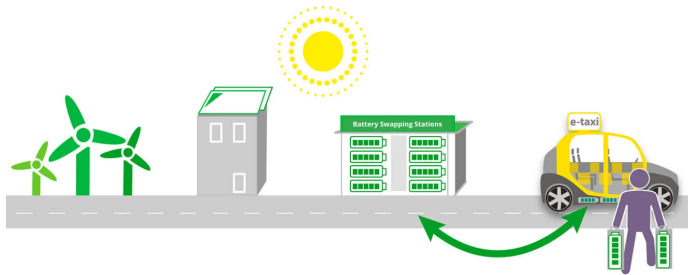


Figure 2.3: Battery swapping [8].

2.2. *CLLC RESONANT CONVERTER*

Lastly, battery swapping shown in Fig.2.3 involves replacing drained vehicle batteries with fully charged ones at swapping stations [9]. On one hand, it offers advantages such as price parity with ICE (internal combustion engine) vehicles, faster recharging, and battery-as-a-service subscription models. It also enables better battery management, grid coordination, and revenue generation. On the other hand, it requires multiple batteries per vehicle leading to material demand and environmental concerns, along with high initial investment costs for swap stations. Additionally, standardization or vehicle-specific stations are needed and the success of battery swapping depends on regional conditions such as policies, market structure, and vehicle applications.

2.2 CLLC Resonant Converter

A valid option for bidirectional isolated DC/DC conversion is the CLLC converter which is attracting more and more attention from research in electric vehicles and energy storage systems due to its high power density and high efficiency. This converter is designed to minimize switching losses, ensuring high efficiency, and enabling operation across a broad voltage range. One notable benefit of the CLLC converter is its effortless attainment of soft switching operation in both forward and reverse modes when subjected to frequency modulation [10].

2.2.1 Types of CLLC Resonant Converter

Four types of converters can be identified based on the morphological structure [11]. The two kinds of switching networks could be full bridges or half bridges while considering the resonant network allows for the choice between a symmetric or asymmetric tank. Various combinations give the four structures represented in Fig. 2.4. All analyses from a mathematical point of view will be conducted in chapter 3.

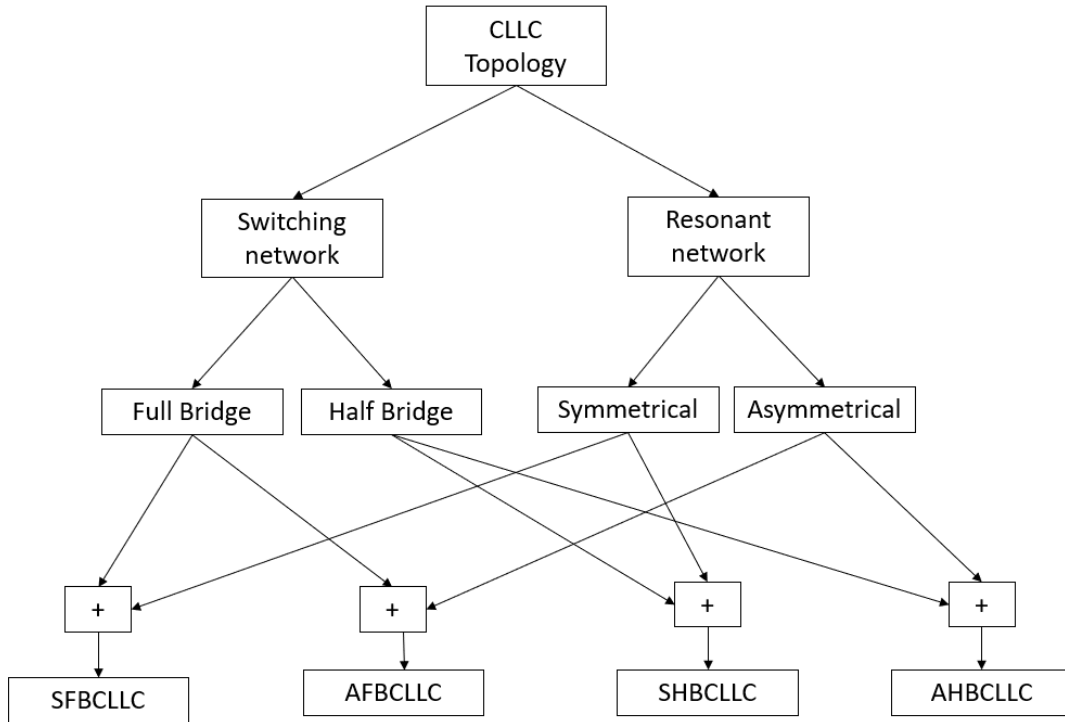


Figure 2.4: Configuration of the four CLLC resonant converters types.

The CLLC converter employs a 4th-order resonant topology and consists of a primary inverting side bridge, a secondary rectifier side bridge, and a resonant tank between them, as shown in Fig. 2.5. The direction of power flow is determined by the desired operation: if the converter participates in grid-to-vehicle (G2V) application, the active bridge on the primary side acts as an inverter, meanwhile, the active bridge on the secondary side serves as a rectifier utilizing synchronous rectification or antiparallel diodes of the transistors when they are in the OFF state. This operation is called also "forward mode". On the other hand, in the case of vehicle-to-grid (V2G) applications the secondary side active bridge inverts the voltage from the batteries and applies it to the resonant tank and this operation is called "reverse mode".

2.2. CLLC RESONANT CONVERTER

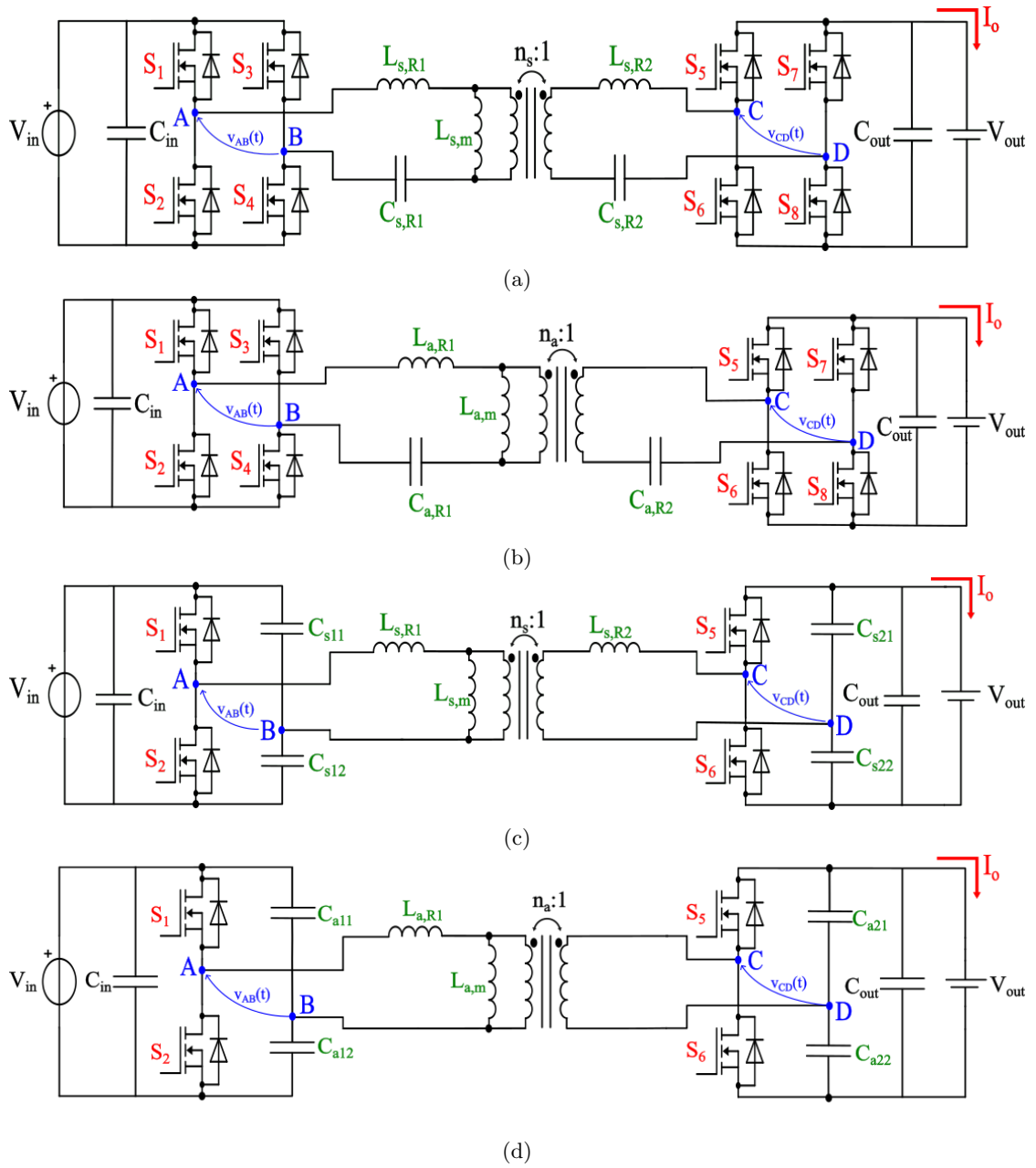


Figure 2.5: Bidirectional CLLC resonant converters: (a) Symmetrical Full Bridge CLLC; (b) Asymmetrical Full Bridge CLLC; (c) Symmetrical Half Bridge CLLC; (d) Asymmetrical Half Bridge CLLC.

The output load, the battery in the case of chargers, is seen in an equivalent way as an equivalent resistance as depicted in Fig. 2.6.

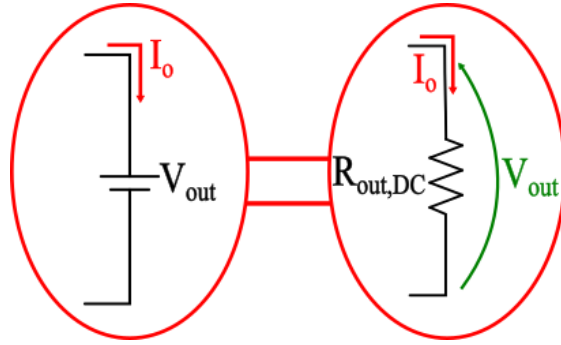


Figure 2.6: Equivalent output resistance.

Referring to the generic case of SFBCLLC, the high-order resonant tank is composed of capacitors $C1$ and $C2$, the transformer magnetizing inductance L_m , and the primary and secondary leakage inductances $L1$ and $L2$. The transformer guarantees the galvanic isolation of the charger. The resonant tank assumes an inductive or capacitive behavior depending on the operating frequency which will determine the buck or boost operation.

2.2.2 Synchronous Rectification

The switches of the two bridges are controlled with square wave signals and a duty cycle of 0.5 as in Fig.2.7. From the literature [12], the rectifier bridge can work in two ways:

- Not controlled, the body diodes conduct;
- Synchronous rectification, an effective method that allows for reducing secondary losses, increasing efficiency.

2.2. CLLC RESONANT CONVERTER

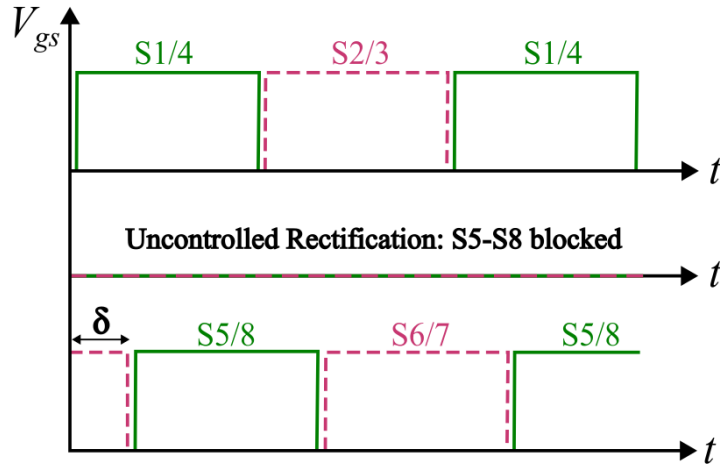


Figure 2.7: Switch command signals.

Determining the phase delay to communicate to the rectifier bridge is not simple. Drawing from the literature [12], there are three potential methods for determining the delay, all represented in Fig. 2.8:

- Device current Detection Method;
- Device voltage sensing;
- Theoretical calculations.

The first method wants switching on synchronized to the sign of the current tanks to a high-frequency current sensor. This method would seem to be the most effective but requires the use of a sensor, implying higher costs.

The second option implies that the rectifier bridge switches are turned on when the V_{ds} (voltage drain-source) is detected $>$ zero and turned off when crosses zero. The problem with this method is represented by a stray inductance which, crossed by the secondary current, takes to zero the V_{ds} before it should.

The last method consists of a calculation of the phase shift using the simplified model of the converter. In the chapter 3 will be proposed a method for the calculation of the phase shift. Unfortunately, this method relies on the FHA (First Harmonic Approximation) which weakens phase prediction for frequencies far from the resonance frequency. To address this issue, reading [13] is recommended, which includes higher-order harmonics, thus increasing the complexity of analytical calculations.

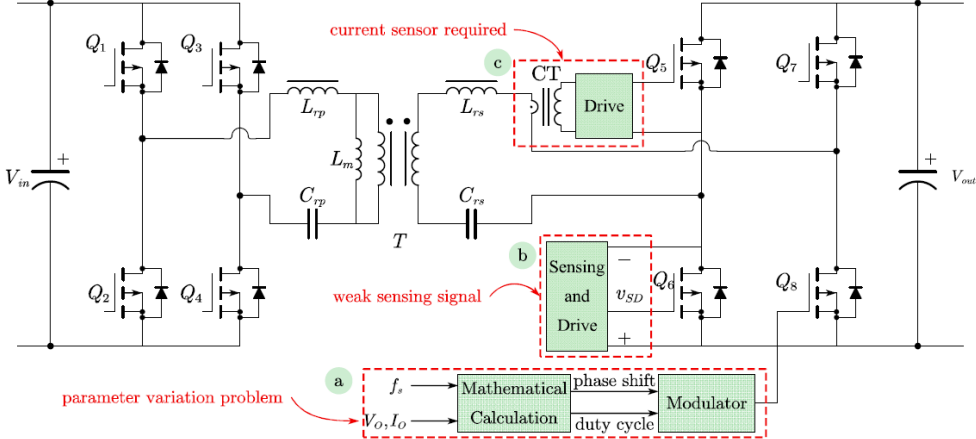


Figure 2.8: SR methods for CLLC converter: (a) theoretical calculation, (b) voltage sensing and (c) current sensing [12].

Chapter 3

Theoretical Analysis and Model

3.1 Equivalent Circuit with FHA

The analytical approach to study the converter starts from simplifying the complex system and conducting analytical studies on an equivalent arrival circuit [11],[14], [15].

First of all, referring to Fig.2.5, it can be noted that the voltages between terminals A and B of the inverting bridge and the voltages between terminals C and D of the rectifier are square waves where the second is shifted by a certain delta positive or negative, represented in Fig.3.1.

By introducing the Fourier theorem, according to which every periodic function can be represented as a linear combination of sinusoidal functions, it's possible to write the voltages of Fig.3.1a as:

$$v_{AB}(t) = \frac{4V_{in}}{\pi} \sum_{n=1,3,5,\dots}^{\infty} \frac{1}{n} \sin(2\pi n f_{sw} t) \quad (3.1)$$

$$v_{CD}(t) = \frac{4V_{out}}{\pi} \sum_{n=1,3,5,\dots}^{\infty} \frac{1}{n} \sin(2\pi n f_{sw} t - \delta) \quad (3.2)$$

On the other hand, for the half-bridge in Fig.3.1b the voltages are halved compared to the previous ones and are:

$$v_{AB}(t) = \frac{4V_{in}}{2\pi} \sum_{n=1,3,5,\dots}^{\infty} \frac{1}{n} \sin(2\pi n f_{sw} t) \quad (3.3)$$

$$v_{CD}(t) = \frac{4V_{out}}{2\pi} \sum_{n=1,3,5,\dots}^{\infty} \frac{1}{n} \sin(2\pi n f_{sw} t - \delta) \quad (3.4)$$

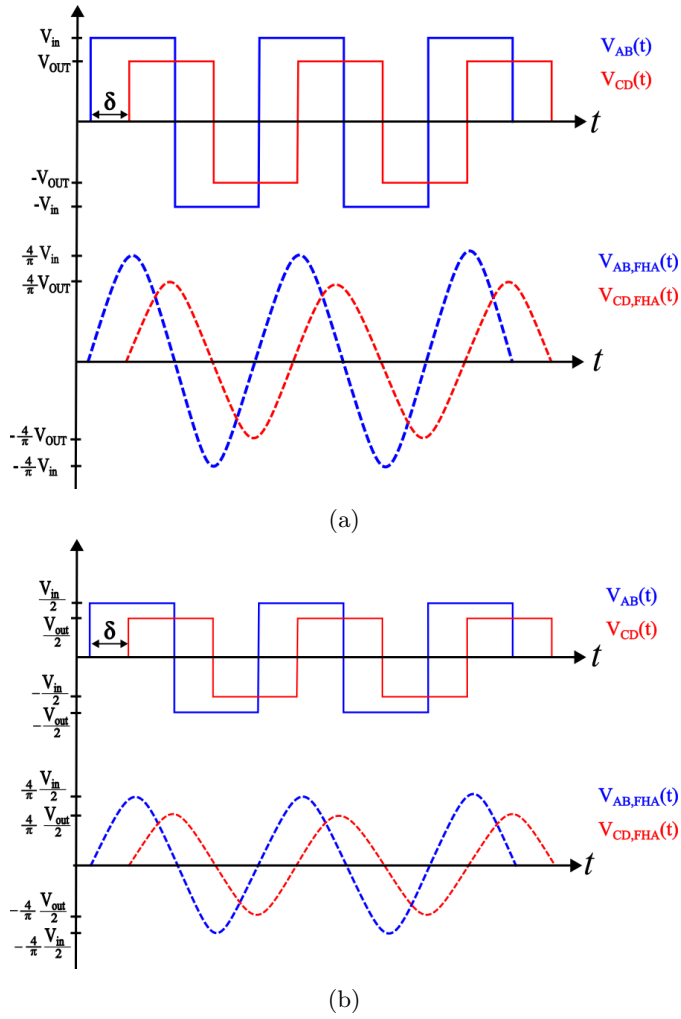


Figure 3.1: Voltages of: (a) Full bridge converter; (b) Half bridge converter.

For the following analytical treatment reference will be made only to the fundamental harmonic employing the First Harmonic Approximation (FHA), even though as the operating frequency moves away from the resonant frequency the accuracy of the hypothesis decreases [13].

By converting the secondary to primary it is possible to refer to the equivalent circuits in Fig.4.22:

3.1. EQUIVALENT CIRCUIT WITH FHA

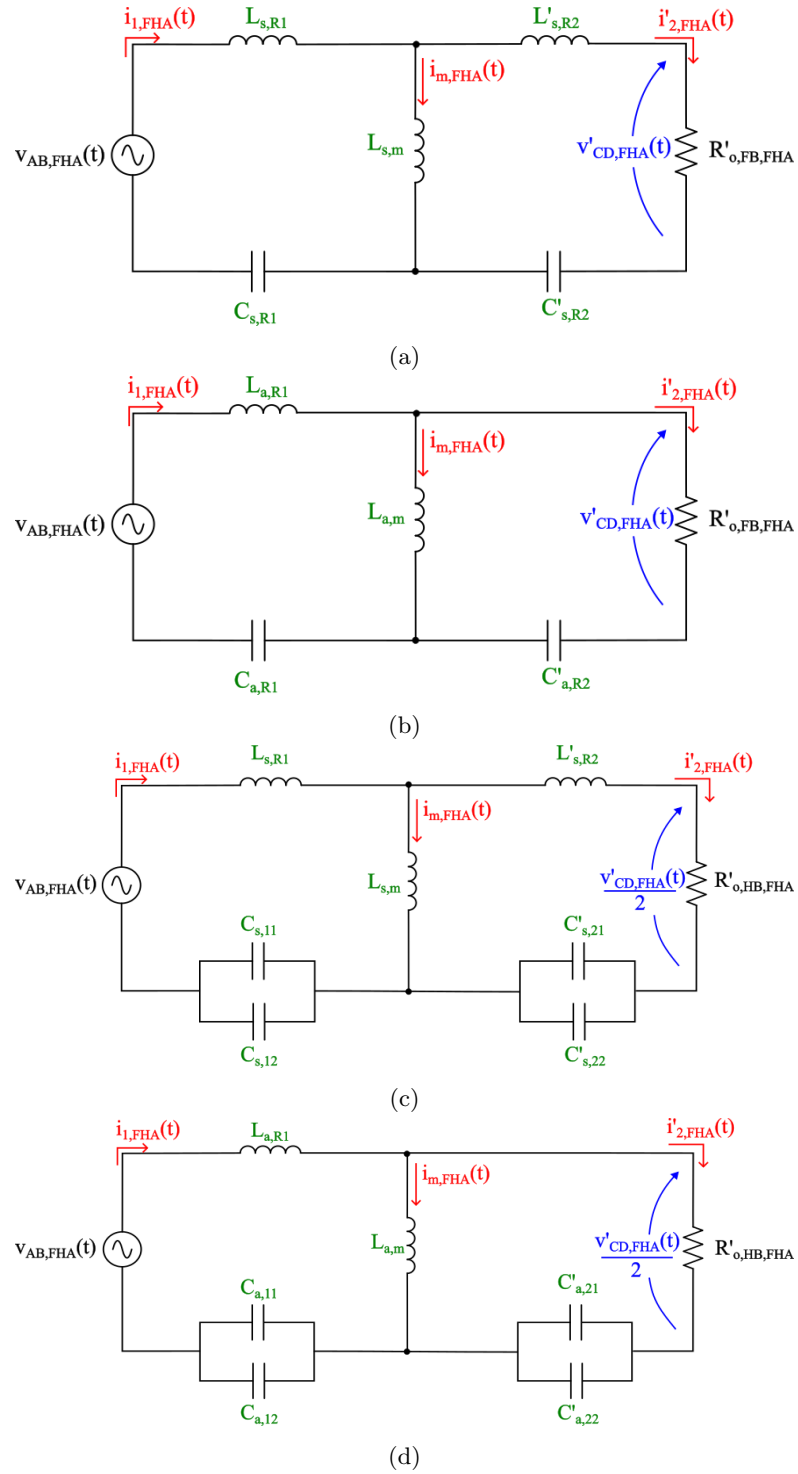


Figure 3.2: Equivalent circuits : (a) Equivalent circuit of SFBCLLC; (b) Equivalent circuit of AFBCLLC; (c) Equivalent circuit of SHBCLLC ; (d) Equivalent circuit of AHBCLLC.

CHAPTER 3. THEORETICAL ANALYSIS AND MODEL

There is a way to equate SCLLC and ACLLC and it is done by assuming that the resonant current (i_1, i_2) and terminal voltage ($v_{AB}v_{CD}$) of SCLLC are the same as those of ACLLC [11]. Thanks to these hypotheses, Some formulas to switch from one structure to another exist which allows referring equivalently to an SCLLC:

$$C_{s,R1} = C_{a,R1} \quad (3.5)$$

$$C_{a,R2} = C_{a,R2} \quad (3.6)$$

$$C_{s,11/s,12} = C_{a,11/a,12} \quad (3.7)$$

$$C_{s,21/s,22} = C_{a,21/a,22} \quad (3.8)$$

$$L_{s,m} = \frac{L_{a,m}}{n_a} \quad (3.9)$$

$$n_s^2 L_{s,2} = \frac{L_{a,m}}{n_a} \left(\frac{1}{n_a} - 1 \right) \quad (3.10)$$

$$L_{s,1} = L_{a,1} + L_{a,m} \left(1 - \frac{1}{n_a} \right) \quad (3.11)$$

In the case of a full bridge in forward mode, the equivalent resistance reported to the primary of the transformer by considering the transformer ratio n_t is calculated as in 3.12.

$$R'_{O,FHA} = \frac{V_{CD,FHA,RMS}}{I_{2,FHA,RMS}} = \frac{2\sqrt{2}V'_{OUT}}{\pi} \frac{1}{\frac{\pi I'_{OUT}}{2\sqrt{2}}} = \frac{8}{\pi^2} \frac{V'_{OUT}}{I'_O} = \frac{8n_t^2}{\pi^2} R_{OUT,DC} \quad (3.12)$$

For the case of Half Bridge always in forward mode, power conservation was used instead and the equation referred to the primary side is in 3.14:

$$\begin{cases} P_{batt} = \frac{V_{OUT}^2}{R_{OUT,DC}} \\ P_{CD} = \frac{n_t^2 V_{CD,RMS}^2}{R'_{O,FHA}} \end{cases} \quad (3.13)$$

Considering $V_{CD,RMS} = \frac{\sqrt{2}V_{OUT}}{\pi}$, the equivalent resistance is obtained as:

$$R'_{O,FHA} = \frac{2n_t^2}{\pi^2} R_{OUT,DC} \quad (3.14)$$

3.1. EQUIVALENT CIRCUIT WITH FHA

In summary, as long as $V'_{CD,FHA,RMS}$ and $I'_{2,FHA,RMS}$ are in phase, the rectifier bridge is equivalent to a resistor that is subjected to sinusoidal waveforms.

There is a further way to refer to a single schematic that unifies all 4. When the magnitudes of DC power supplies is V_{in} and the output voltage is V_{out} the equivalent input and output voltages of the FBCLLC and HBCLLC can be expressed as $\pm mV_{in}$ and $\pm mV_{out}$, with $m = 1$ for FBCLLC and $m = 1/2$ for HBCLLC.

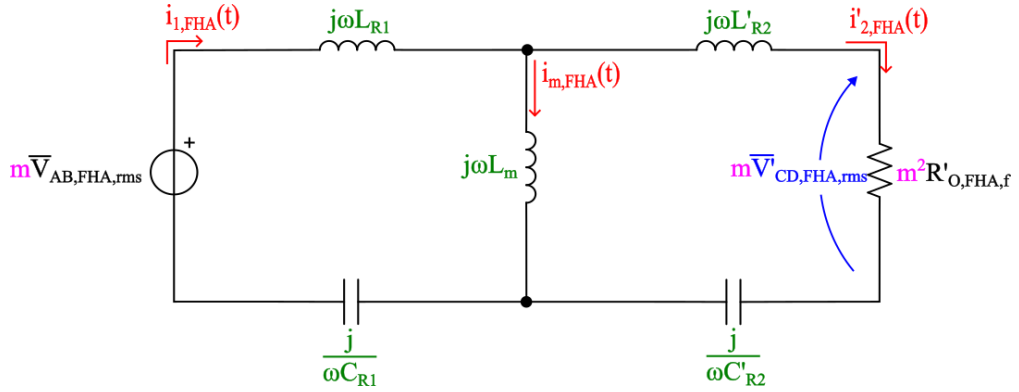


Figure 3.3: Unified equivalent circuit in forward mode.

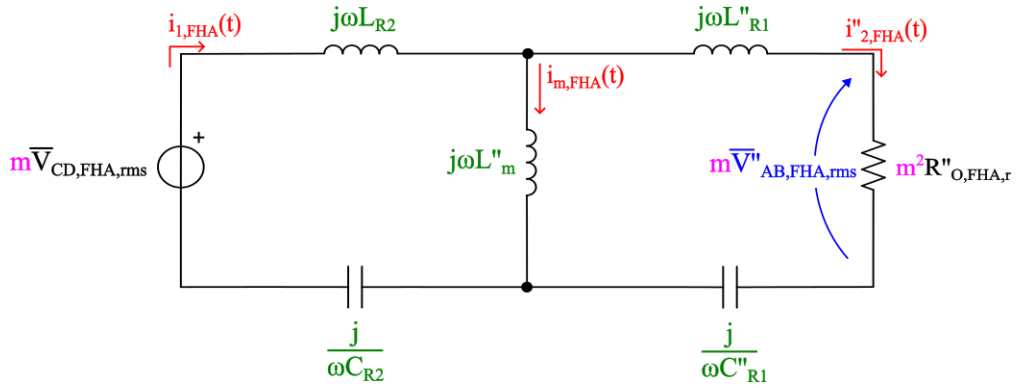


Figure 3.4: Unified equivalent circuit in reverse mode.

From this point on, reference will be made to the equivalent circuit of the SFB-CLLC, because of its status as the most efficient configuration given identical converter specifications, as highlighted in [11].

3.2 Gain Analysis

As long as all elements are subjected to the same frequency, the phasor method is employed to analyze the circuit in the frequency domain.

By referring to the equivalent circuit of SFBCLLC in Fig.3.2a the gain with FHA of the converter in forward mode operation is found as:

$$H = \frac{V'_{CD,FHA}}{V_{AB,FHA}} \quad (3.15)$$

By performing all calculations outlined in A, the result is reported in 3.16.

$$H(j\omega_n, Q) = \frac{1}{\left(\frac{1}{k} - \frac{1}{\omega_n^2 k} + 1\right) + j \left[Q\omega_n \left(1 + \frac{a}{k} + a\right) - \frac{Q}{\omega_n} \left(\frac{1}{kb} + \frac{a}{k} + \frac{1}{b} + 1\right) + \frac{Q}{kb\omega_n^3} \right]} \quad (3.16)$$

The module of 3.16 is calculated in 3.17:

$$M(j\omega_n, Q) = \left\{ \left(\frac{1}{k} - \frac{1}{\omega_n^2 k} + 1\right)^2 + \left[Q\omega_n \left(1 + \frac{a}{k} + a\right) - \frac{Q}{\omega_n} \left(\frac{1}{kb} + \frac{a}{k} + \frac{1}{b} + 1\right) + \frac{Q}{kb\omega_n^3} \right]^2 \right\}^{-\frac{1}{2}} \quad (3.17)$$

Where the following parameters have been introduced:

$$\omega_{R1} = \frac{1}{\sqrt{L_{s,R1} C_{s,R1}}} \quad (3.18)$$

$$\omega_n = \frac{\omega_s}{\omega_{R1}} \quad (3.19)$$

$$k = \frac{L_m}{L_{R1}} \quad (3.20)$$

$$Z_0 = \sqrt{\frac{L_{R1}}{C_{R1}}} \quad (3.21)$$

$$Q = \frac{Z_0}{R'_o} \quad (3.22)$$

$$a = \frac{L'_{R2}}{L_{R1}} \quad (3.23)$$

$$b = \frac{C'_{R2}}{C_{R1}} \quad (3.24)$$

3.2. GAIN ANALYSIS

Where the following simplifications have been introduced:

$$L_{R1} = L_{s,R1} ; L'_{R2} = L'_{s,R2} ; L_m = L_{s,m} ; C_{R1} = C_{s,R1} ; C'_{R2} = C'_{s,R2} ; R'_o = R'_{o,FB,FHA}$$

The definition of Q is closely related to the load condition R'_o and will be extensively examined in the 4 chapter. At this point, it suffices to notice that the transfer function, besides being dependent on the operating frequency, also relies on the load conditions, as illustrated in Fig.3.5.

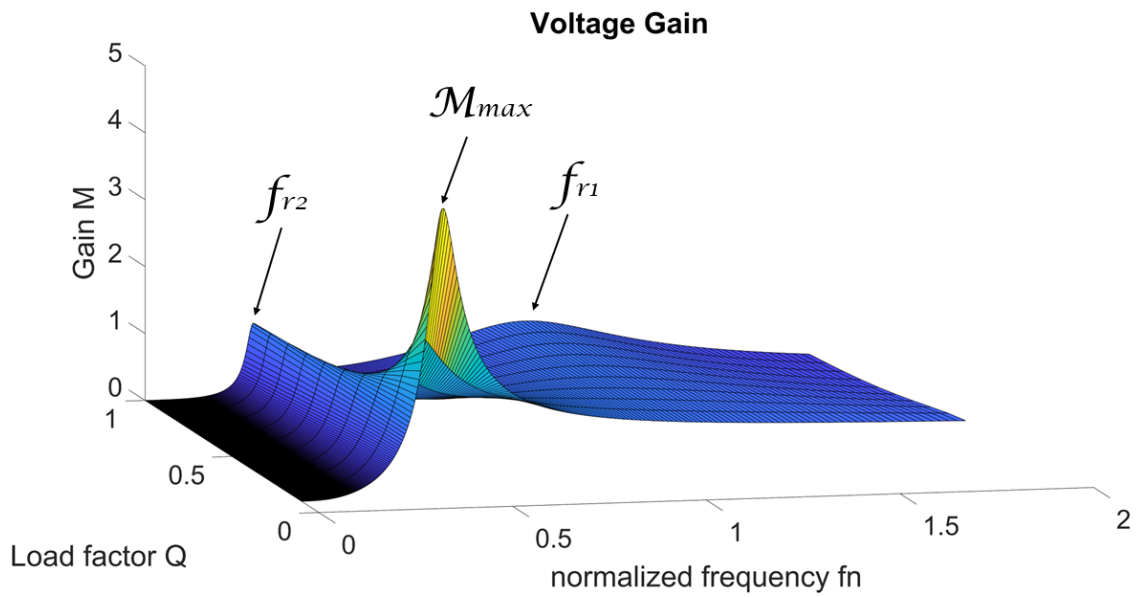


Figure 3.5: Transfer function of CLLC.

In Fig.3.5, the two resonance frequencies f_{r1} and f_{r2} are visible and are defined as in 3.25. Furthermore, it can be seen that for zero load ($Q = 0$) the maximum gain M_{max} is reached.

$$\begin{cases} f_{r1} = \frac{1}{2\pi\sqrt{L_{r1}C_{r1}}} \\ f_{r2} = \frac{1}{2\pi\sqrt{(L_{r1} + L_m)L_{r1}}} \end{cases} \quad (3.25)$$

3.3 ZVS Region Boundary

To maintain soft switching conditions, it is advisable to ensure that the circuit operates in an inductive condition. This analysis was conducted by studying the sign of the imaginary part of the impedance of the equivalent circuit as seen at the input terminals [16].

$$\begin{aligned} Z_1 &= j\omega_s L_{R1} + \frac{1}{j\omega_s C_{R1}} \\ Z_2 &= j\omega_s L'_{R2} + \frac{1}{j\omega_s C'_{R2}} \\ Z_m &= j\omega_s L_m \end{aligned} \quad (3.26)$$

where, to simplify the notations the following parameters have been imposed:

$$L_{R1} = L_{s,R1} ; L_{R2} = L'_{s,R2} ; L_m = L'_{s,m} ; C'_{R1} = C'_{s,R1} ; C'_{R2} = C'_{s,R2} ; R'_o = R'_{o,FB,FHA}$$

For the CLLC resonant converter, the input impedance is calculated in C where has been found:

$$Z_{in} = R'_o \left(\frac{Q^2 - \omega_n^2 Q^2 (ab + kb + k + 1) + \omega_n^4 Q^2 (ab + kb + kab) + jQb(\omega_n - \omega_n^3(1+k))}{-\omega_n^2 b + j\omega_n Q[1 - \omega_n^2 b(a+k)]} \right) \quad (3.27)$$

In which the parameters defined in 3.18, 3.19, 3.20, 3.21, 3.22, 3.23, 3.24 have been used.

To find the $Im(\angle Z_{in})$, some manipulations of the formula 3.27 have been performed, like imposing the following parameters:

$$c = Q^2 - \omega_n^2 Q^2 (ab + kb + k + 1) + \omega_n^4 Q^2 (ab + kb + kab) \quad (3.28)$$

$$d = Qb(\omega_n - \omega_n^3(1+k)) \quad (3.29)$$

$$e = -\omega_n^2 b \quad (3.30)$$

$$f = \omega_n Q[1 - \omega_n^2 b(a+k)] \quad (3.31)$$

$$Z_{in} = R'_o \frac{c + jd}{e + jf} = R'_o \frac{ce + df - j(cf - de)}{e^2 + f^2} = R'_o \frac{ce + df}{e^2 + f^2} + j \frac{-R'_o(cf - de)}{e^2 + f^2} \quad (3.32)$$

By imposing $Im(\angle Z_{in})$ equal to zero, has been found the 3.33 equation:

3.3. ZVS REGION BOUNDARY

$$Q_{lim} = \sqrt{\frac{\omega_n^4(1+k) - \omega_n^2}{(1 - \omega_n^2(2k+2) + \omega_n^4(2k+1))(1 - \omega_n^2(k+1))}} \quad (3.33)$$

The 3.33 equation has been substituted in the Gain Voltage formula 3.17 and represented graphically in Fig.3.6. From the substitution the red curve has been obtained, present only in the half-plane to the left of the resonance frequency. This means that in URFM (upper resonant frequency mode) operation ($f_{sw} > f_{r1}$) each operating point operates in the inductive region. On the other hand, for LRFM (low resonant frequency mode) operation ($f_{sw} < f_{r1}$) it must always stay above the red curve.

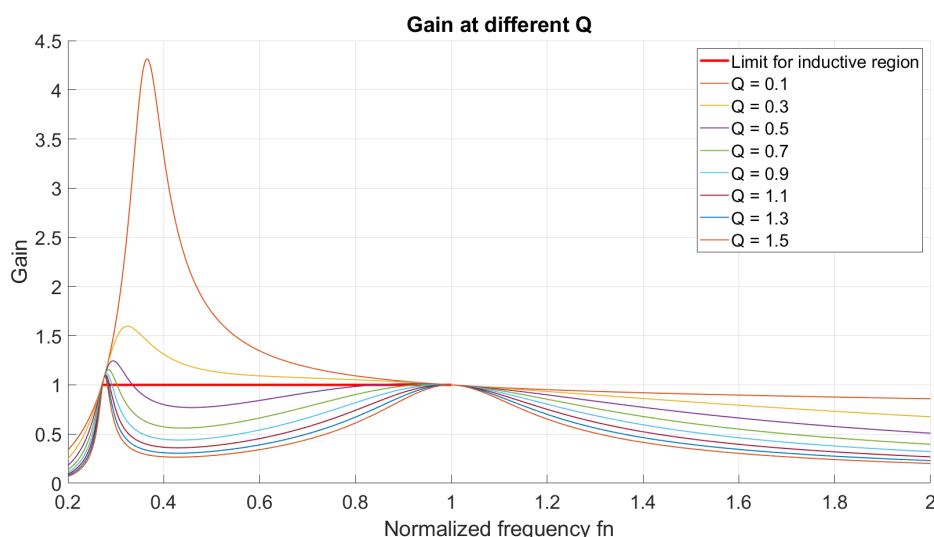


Figure 3.6: Inductive limit for ZVS operation.

From a control point of view, there is an interest in remaining within the inductive region to ensure stable control of the output voltage. Using a PI controller, the correction in terms of voltage is proportional to the error value. As shown in Fig. 3.7, if the output voltage decreases following small disturbances, Q increases, moving from the operating point A to B. Following a negative error, the PI controller produces a frequency command lower than the initial one moving to point C. At point C, the output voltage is greater than the reference voltage at point A; therefore, a frequency command higher than the frequency at C is generated. The converter will operate at point D until iterating, where it will work at point F with the same voltage as point A before the disturbance.

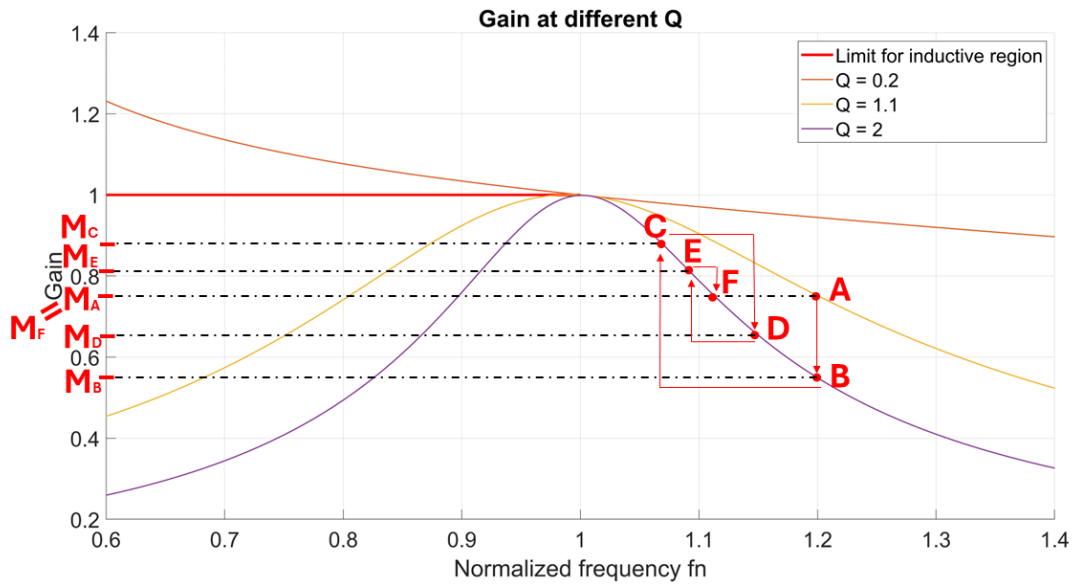


Figure 3.7: Operation in the inductive region.

On the other hand, looking at Fig.3.8, for greater disturbances the converter will work again at point B. In this case, however, the PI controller will generate a much lower frequency command compared to the starting point by going to point C. Since the output voltage is still lower than the reference one, the controller will continue to decrease the frequency command. The converter therefore becomes unstable when it goes to work in the capacitive region where the gain slope is positive.

3.4. PHASE SHIFT ESTIMATION

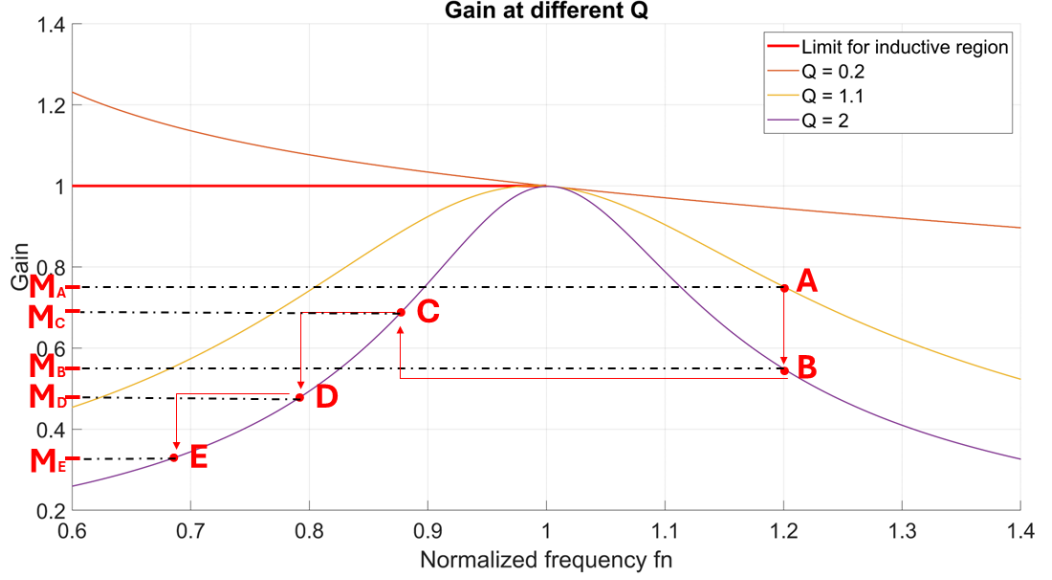


Figure 3.8: Operation in the capacitive region.

3.4 Phase Shift Estimation

Since there is a resistance at the output, the current and voltage on that resistance are in phase. The objective of the synchronous rectification (SR), as seen in Chapter 2.2.2, is to synchronize the opening of the switches in the rectifier bridge with the phase of the secondary current. In addition, the phase of the current in the equivalent circuit is the same as the voltage across the resistance. Therefore, the calculation of the phase of the transfer function was performed ($\angle H(j\omega_n, Q)$) considering the phase of the primary bridge generator as the reference phase. By referring to 3.16 and defining A and B as in 3.34, the phase calculation is reported in table 3.1.

$$\begin{cases} A &= \frac{1}{k} - \frac{1}{\omega_n^2 k} + 1 \\ B &= Q\omega_n \left(1 + \frac{a}{k} + a\right) - \frac{Q}{\omega_n} \left(\frac{1}{kb} + \frac{a}{k} + \frac{1}{b} + 1\right) + \frac{Q}{kb\omega_n^3} \end{cases} \quad (3.34)$$

$A = 0 \ \& \ B < 0$	$ph = \frac{\pi}{2}$
$A = 0 \ \& \ B > 0$	$ph = -\frac{\pi}{2}$
$A > 0$	$ph = \arctan(\frac{-B}{A})$
$A < 0 \ \& \ B \leq 0$	$ph = \arctan(\frac{-B}{A}) + \pi$
$A < 0 \ \& \ B > 0$	$ph = \arctan(\frac{-B}{A}) - \pi$

Table 3.1: Calculation of phase shift.

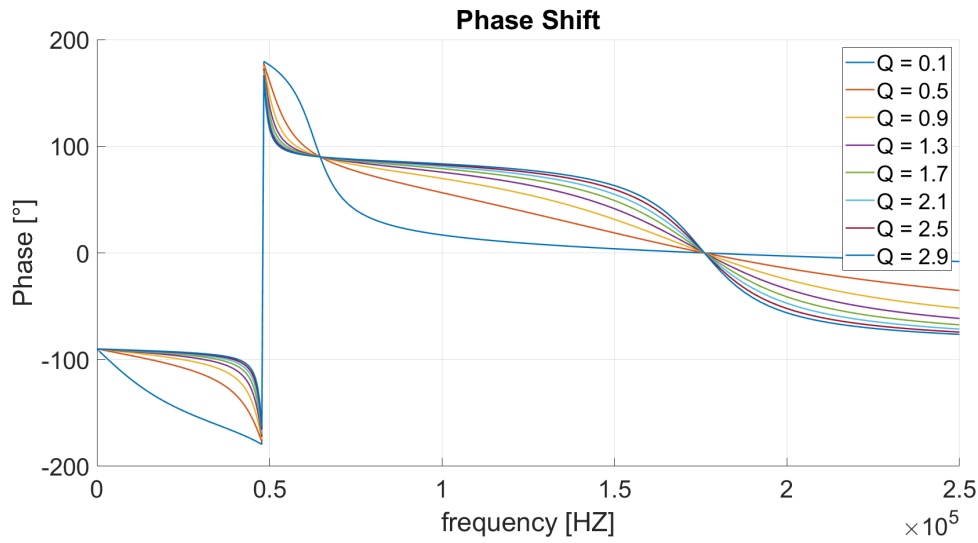


Figure 3.9: Phase shift from theoretical calculations.

In Fig.3.9, the phase calculation at various load conditions as a function of frequency is depicted. Furthermore, to have a modeling correspondence, a rapid simulation was performed on LTspice (Fig. 3.10), and the phase of the V_{out} node represented in Fig.3.11 was extrapolated.

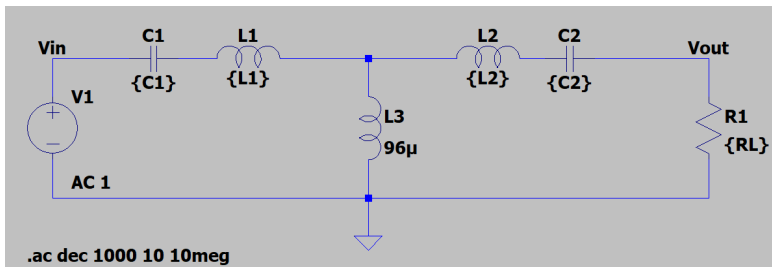


Figure 3.10: CLLC equivalent circuit modeled on LTspice.

3.4. PHASE SHIFT ESTIMATION

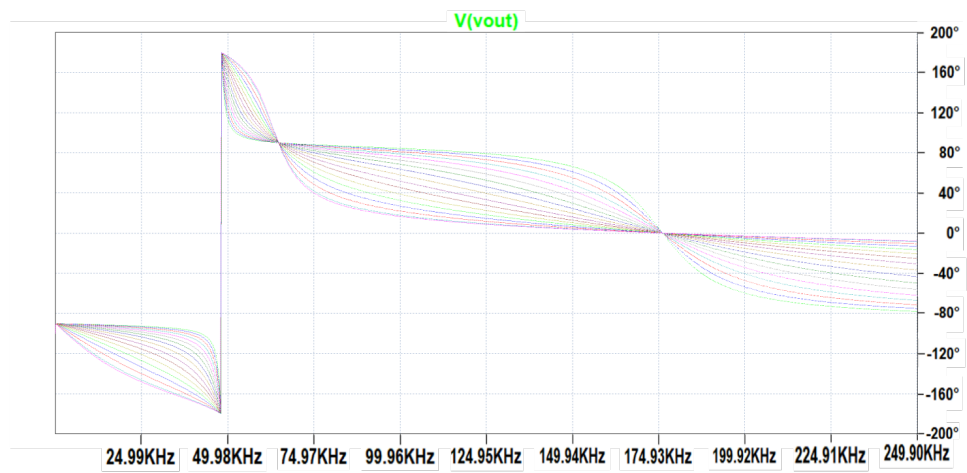


Figure 3.11: Phase shift from LTspice.

CHAPTER 3. THEORETICAL ANALYSIS AND MODEL

Chapter 4

Plecs Simulations Results

To arrive at the simulation of the real CLLC a step-by-step process was undertaken beginning with the simplified model of the equivalent resistance, which represents the culmination of the theoretical analysis conducted in Chapter 3, and progressing to the final complete model of the CLLC.

The values used in the simulations are taken from an already existing converter and are reported in table 4.1.

L_{R1}	$15.2 \mu H$
L_{R2}	$9.9 \mu H$
C_{R1}	$54 nF$
C_{R2}	$91.6 nF$
L_m	$96 \mu H$
n_t	$24/19$
f_{R1}	$175 kHz$
Z_0	$16.8 ohm$

Table 4.1: Parameters of CLLC.

4.1 Equivalent Output Resistance Model

The objective of the following simulation is to verify if the phase shift formula in 3.1, which will be used to synchronize the output bridge switches of the real model, is correct.

The parameters used in Fig. 4.1 have been reported to the primary side of the transformer considering the transformer ratio n_t . According to the FHA, the input V_{in} is sinusoidal, to subject the circuit to the fundamental harmonic only.

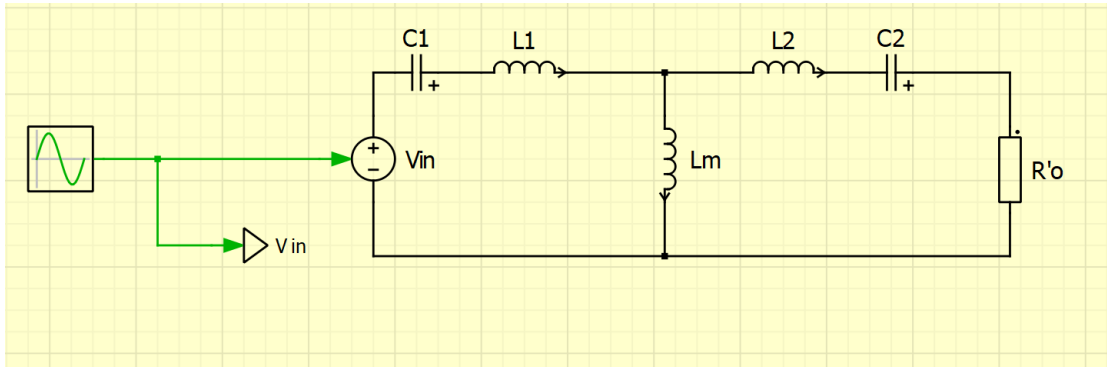


Figure 4.1: Equivalent resistance model.

In this simulation, the equivalent output resistance and the operating frequency are cyclically imposed. Subsequently, given that the phase shift formula $ph = ph(Q, f_{sw})$ is a function of the load factor and the frequency (cf. 3.1) and knowing the relation of the load factor $Q = \frac{Z_0}{R'_0}$, it is possible to determine the theoretical delay between the input voltage and the output voltage across the resistor.

To verify that the obtained values are correct, a method through simulation is proposed. From the model the input and output voltage signals are taken and sent to the "hit crossing" blocks, as represented in Fig.4.2. From this block, a pulse signal equal to 1 is generated when the respective sinusoidal wave signal crosses zero and then enters into the "Phase shift integrator" subsystem, shown in Fig.4.3.

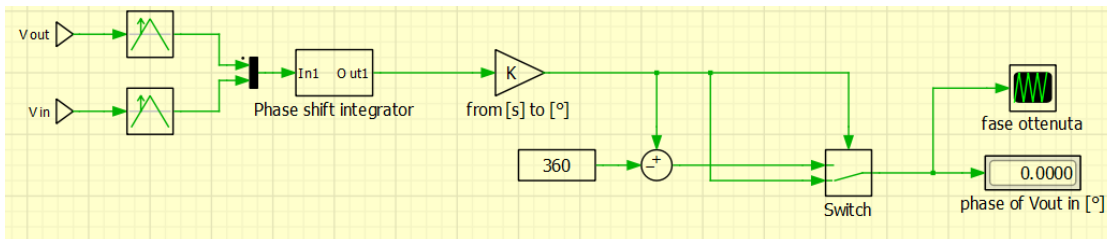


Figure 4.2: Diagram of the phase shift calculation.

Looking at Fig.4.3, the signals from the "hit crossing" blocks are sent to the "flip-flop" block, which is activated when it receives the first signal (S) and remains equal to 1 until the second signal (R) arrives. At the output, there will be a signal equal to 1 as long as the delay between the two signals lasts. By integrating the delay, the measurement of the delay in seconds is obtained and represents the output of the subsystem. Subsequently, the signal is converted into degrees and saturated at 360° .

4.1. EQUIVALENT OUTPUT RESISTANCE MODEL

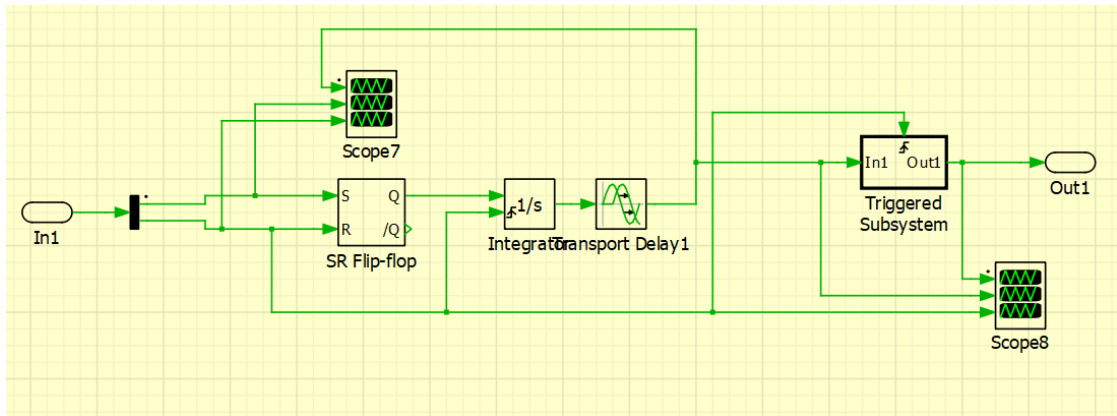


Figure 4.3: "Phase shift integrator" block.

The acquired data from the theoretical calculation and the simulation's calculation have been compared and shown in Fig.4.4, where, for each simulated point, the values appear to coincide.

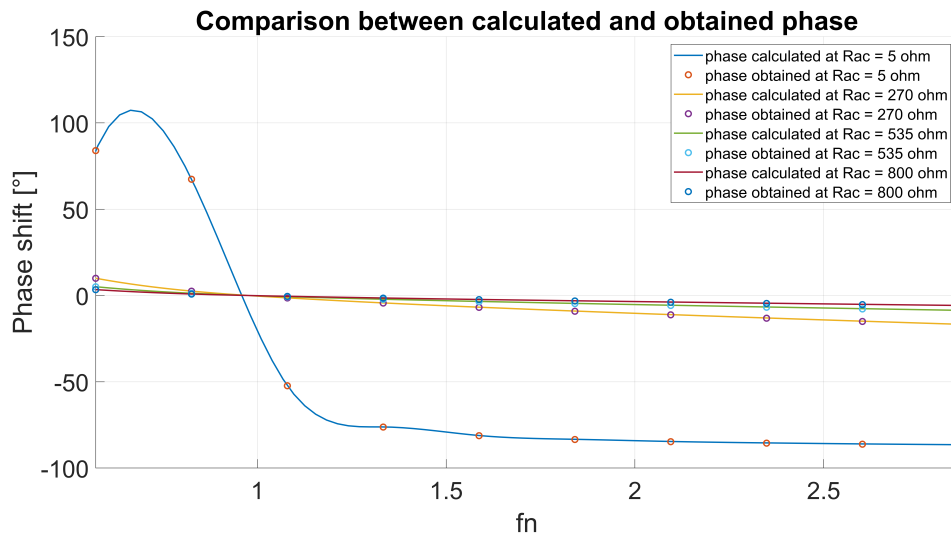


Figure 4.4: Comparison between calculated and obtained phase.

But, to get an idea of how much the two datasets differ, Fig.4.5 shows the error between the two, reaching a maximum of 0.18° for frequencies 2.5 times higher than the resonance frequency f_{R1} . Furthermore, it is also obtained that the error between the two forms of calculation is independent of the type of output, but will depend only on the frequency.

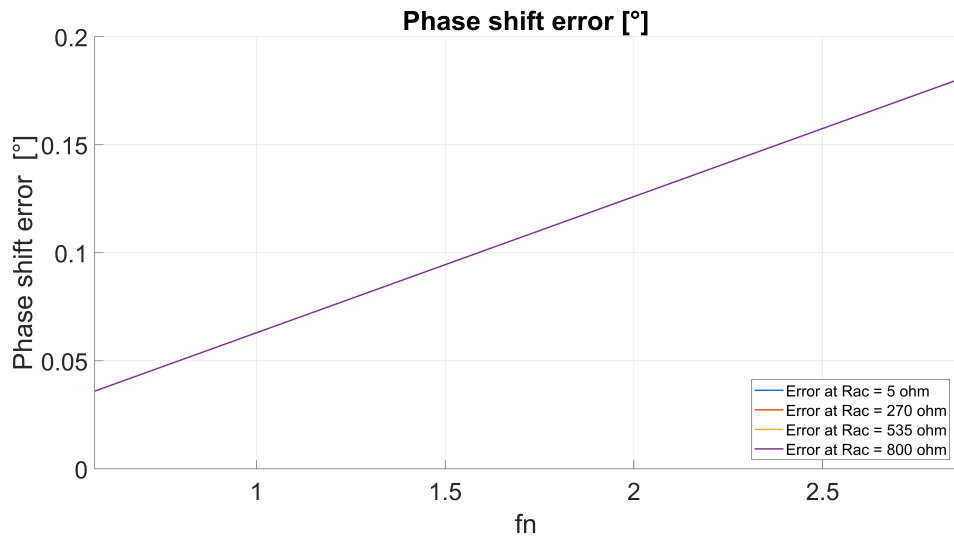


Figure 4.5: Error between theoretical and obtained phase shift.

In conclusion, the error between the two forms of calculation is minimal with a maximum of 0.18° . So, from now on, the theoretical phase shift formula will be used without making large errors.

4.2 Sinusoidal Model

In the following model, the output resistor is removed and replaced by a sinusoidal input voltage generator, going to add another variable.

4.2. SINUSOIDAL MODEL

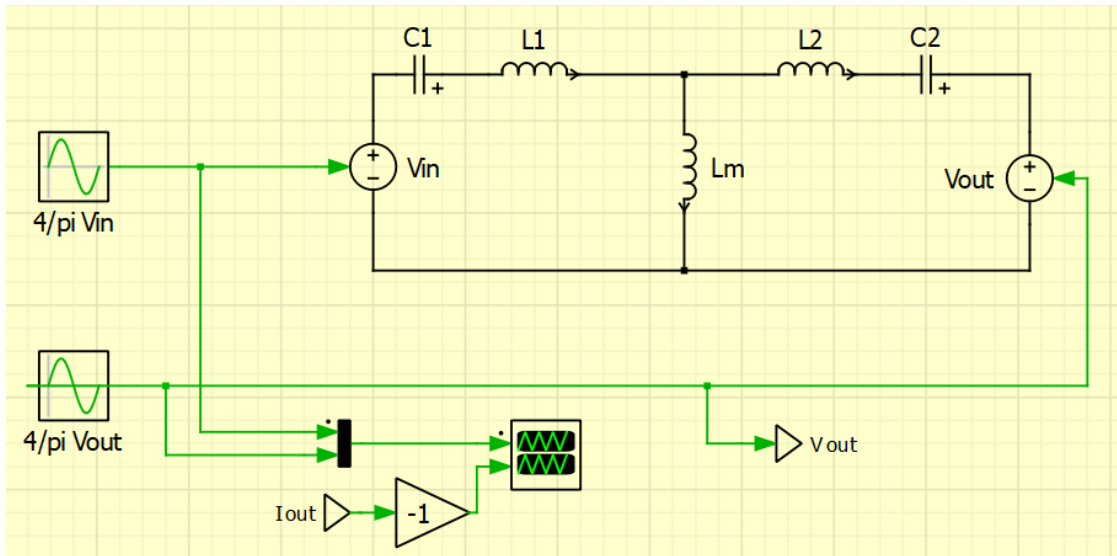


Figure 4.6: Sinusoidal model.

4.2.1 Sinusoidal Model Validation

The goal of the model is to verify that the converter behaves as expected. In fact, a certain value of the equivalent resistance R'_o is imposed, from which the value of the load factor Q is calculated. A certain Q and a certain switching frequency f_{sw} are cyclically imposed to the model and the delay with which the output generator is shifted with respect to the input voltage is calculated. The formula used is the one that was validated in the paragraph 4.1, as well as that found theoretically.

In calculating the amplitude of the sinusoidal voltage of the generator, the procedure involves advancing through the mathematical model. The gain formula derived from the theoretical analysis is applied, by knowing the operating frequency and the load factor, after which the calculation of V_{out} is conducted as $V_{out} = M \cdot V_{in}$, according to the definition of voltage gain, where the input voltage is imposed by the model.

Once all the values to be given in command to the model are known, the simulation starts.

The objective is to ensure that the equivalent output resistance R'_o as a consequence of parameters derived from analytical calculations matches the initially set value.

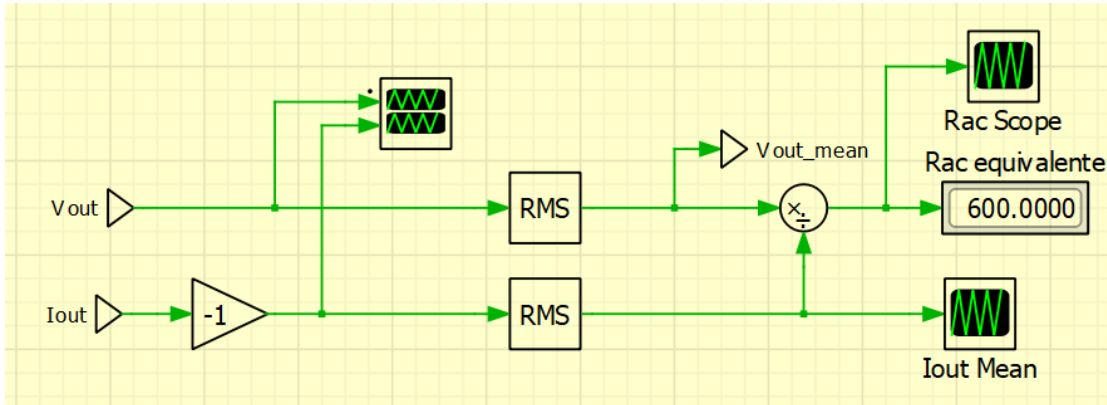


Figure 4.7: Calculation of equivalent output resistance in the sinusoidal model.

To calculate the equivalent resistance in the simulation, cf. Fig.4.7, is carried out by applying the theoretical formula outlined in eq.3.12. In fact, by definition, the output resistance is equal to the ratio of the RMS values of the voltage and current input to the rectifier bridge. In this simplified model they correspond to the voltage imposed by the generator and the current passing through it. By referring to the schematic in Fig.4.7, the gain equal to -1 was introduced to use the user's convention.

As a result, all the values obtained from the simulation method coincide exactly with the output resistance value imposed on the model.

4.2.2 Sinusoidal Model Working Points Map

Once the correct functioning of the model was verified, a second simulation was carried out, to sweep more operating frequencies and operating gains. From this simulation, the various load factors obtained are compared with the theoretical ones. Finally, the currents and powers absorbed by the equivalent output load for each operating point are mapped.

First of all, by cyclically imposing an operating frequency and an output voltage, and consequently also the gain, is possible to obtain the load factor. Indeed, the gain $M = f(Q, f_{sw})$ is a function of Q and f_{sw} , so the load factor Q can be found from the inverse relationship. The equation of the gain in 3.17 is expressed as 4.1 :

$$M = \frac{1}{\sqrt{A^2 + Q^2 C^2}} \quad (4.1)$$

4.2. SINUSOIDAL MODEL

where A and C are defined to simplify as 4.2 and 4.3:

$$A = \frac{1}{k} - \frac{1}{\omega_n^2 k} + 1 \quad (4.2)$$

$$C = \omega_n \left(\frac{a}{k} + a + 1 \right) - \frac{1}{\omega_n} \left(\frac{a}{k} + \frac{1}{kb} + \frac{1}{b} + 1 \right) + \frac{1}{\omega_n^3 kb} \quad (4.3)$$

The load factor is derived as:

$$Q = \frac{\sqrt{\frac{1}{M^2} - A^2}}{C^2} \quad (4.4)$$

The regions of existence of the root are satisfied by the following relation:

$$\frac{1}{M^2} - A^2 \geq 0 \quad (4.5)$$

From which the limit gain equation 4.6 is obtained for each operating frequency by imposing the minimum possible load factor $Q = 0$:

$$M_{lim} = \frac{1}{\frac{1}{k} - \frac{1}{\omega_n^2 k} + 1} \quad (4.6)$$

Here, once the switching frequency f_{sw} and the load factor are known, the phase delay $ph = ph(Q, f_{sw})$ to be applied to the output generator is determined.

At this stage, all parameters required for the simulation are known, thus initiating a 40x40 grid map and displaying the results.

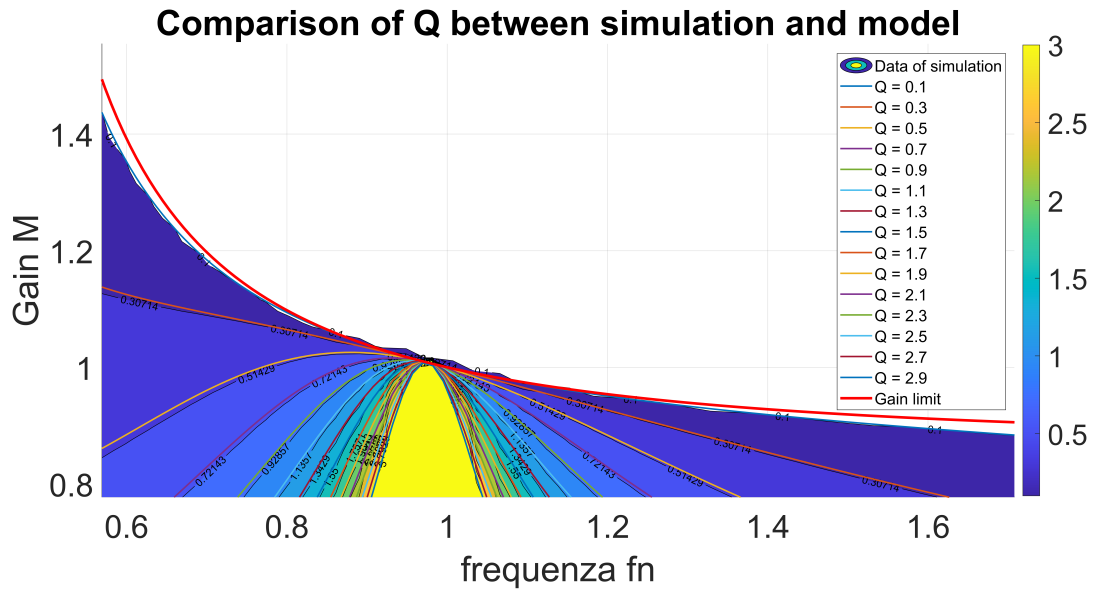
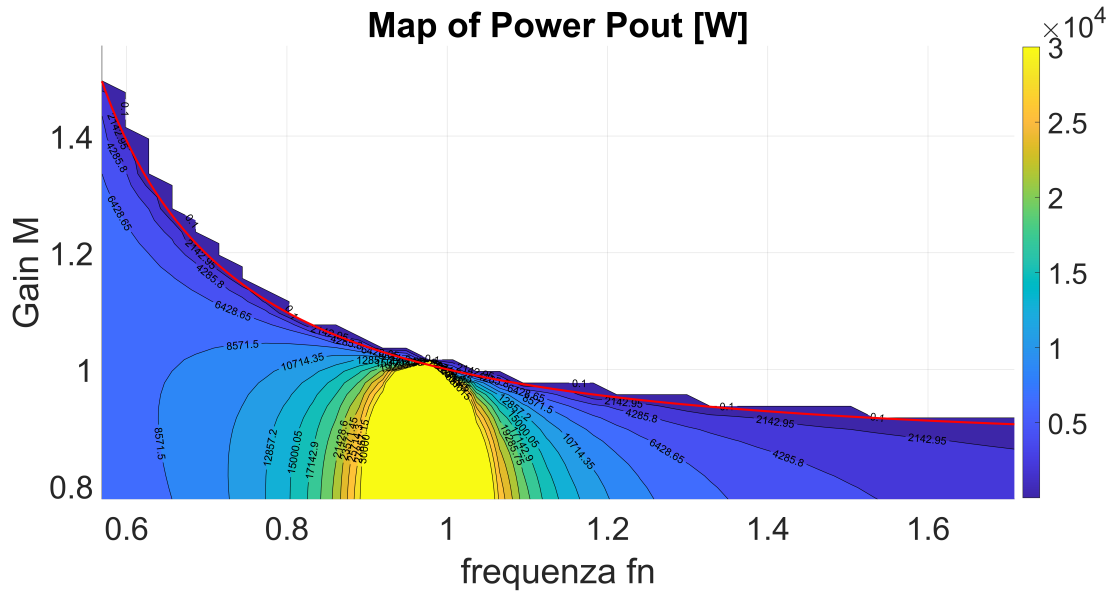


Figure 4.8: Comparison of voltage gain between the theoretical model and the obtained results in the sinusoidal model.

Fig. 4.8 shows the comparison between the gain at different load factors Q from the theoretical analysis and those recorded by the point-by-point simulation, in a map of 40×40 points.

The plot was obtained initially by doing a filled contour plot containing the isolines of the matrix Q taken from the PLECS simulation, where Q contains height values on the $f_{sw}-M$ plane. The filled contours are the regions colored on the scale from yellow to blue in Fig.4.8. Then, the Q -isolines of the theoretical equation of the Gain 3.17 are overlaid on the previous graph and are the colored lines represented in the same figure.

It can be seen how the iso-curves of the load factor are fairly respected and also how the estimate of the maximum gain 4.6 at $Q = 0$ is predicted correctly. Indeed all the operating points are below the red line in Fig.4.8.



4.3. SQUARE WAVE MODEL

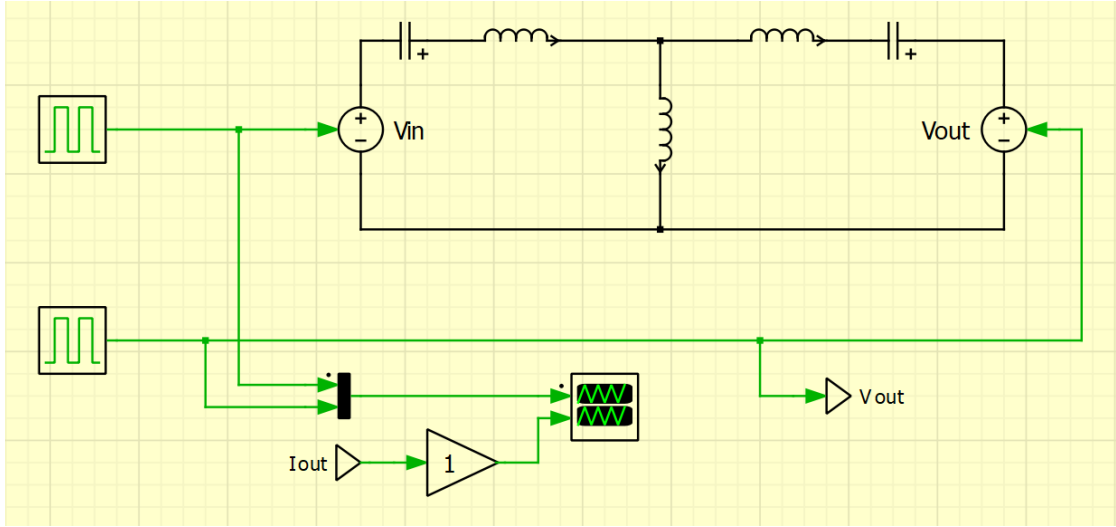


Figure 4.11: Square wave model.

4.3.1 Square Wave Model Validation

Comparing the behavior of the square wave model concerning the sinusoidal one is the objective of a first simulation, to determine what error is made by introducing all the other harmonics.

The simulation requires defining a vector of desired equivalent resistances and subsequently calculating the necessary parameters for running the simulation. Once these parameters are established, the obtained values are compared to the desired ones.

The method for deciding the voltage to power the output, in terms of amplitude and delay compared to the input generator, is the same as what has been done in the paragraph of the verification of the sinusoidal model 4.2.1.

What changes is how the output equivalent resistance R'_{o} is now calculated in the model. According to the definition 3.12, $V_{CD,FHA,RMS}$ is calculated as $\frac{2\sqrt{2}}{\pi}V'_{out}$, while the $I_{2,FHA,RMS}$ was obtained by letting the output current I'_{out} enter the RMS block, as shown in Fig.4.12.

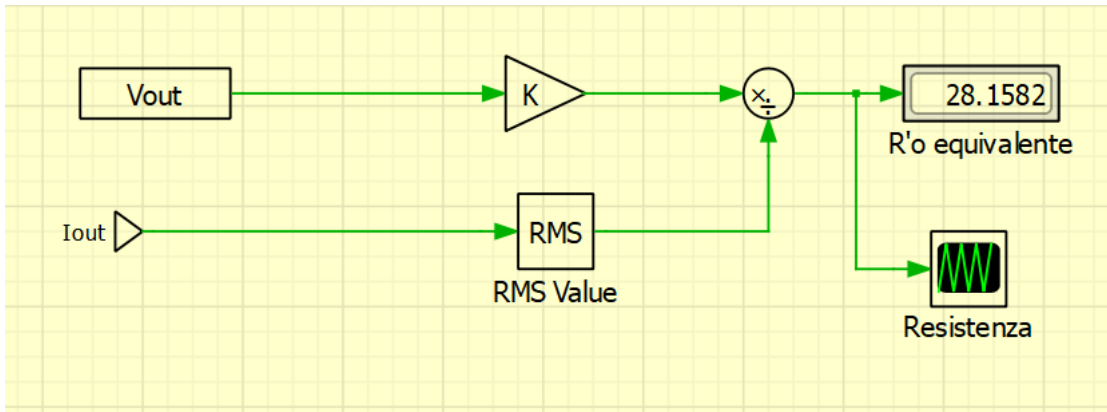


Figure 4.12: Calculation of equivalent output resistance in square wave model.

By testing some resistance values at multiple operating frequencies, the results shown in Fig.4.13 were obtained, where the continuous lines are the obtained values from the model, while the dashed lines are the imposed values.

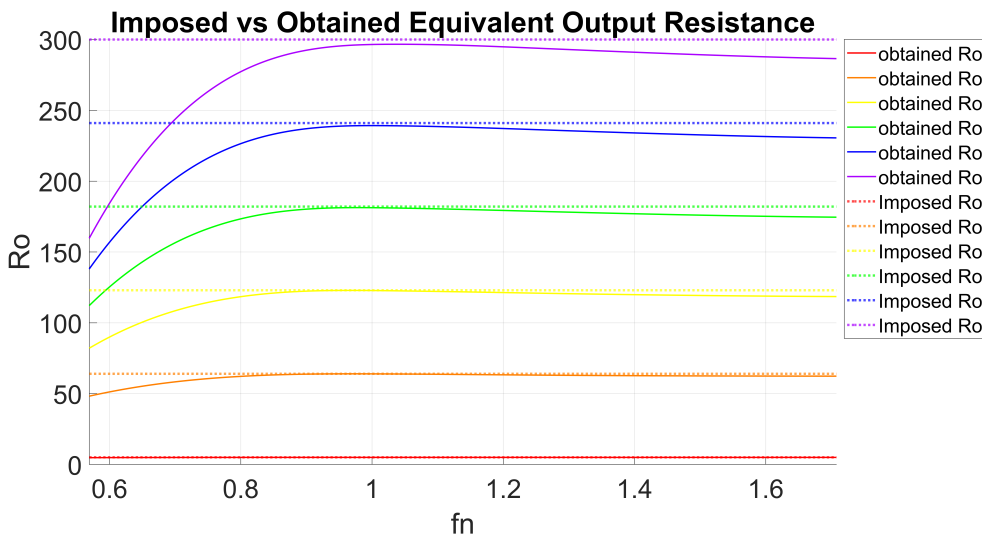


Figure 4.13: Comparison between the imposed and obtained equivalent output resistance in square wave model.

From a general analysis of Fig.4.13, it is possible to notice that at low frequencies there is a greater difference between the imposed value and the one obtained. Furthermore, as the output equivalent resistance value increases, the error at low frequencies increases. To get an idea of what the error is, in Fig.4.14 the relative percentage error is shown.

4.3. SQUARE WAVE MODEL

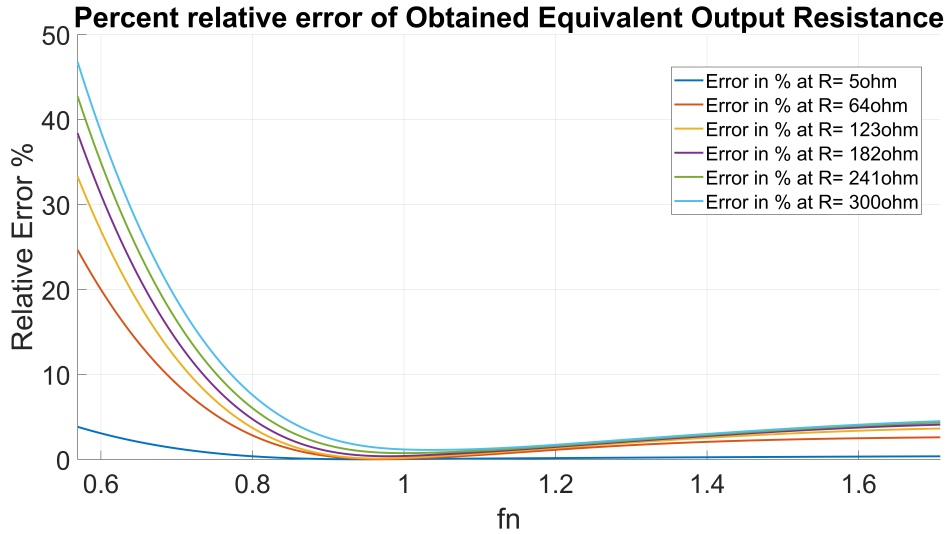


Figure 4.14: Relative percentage error between the imposed and obtained equivalent output resistance in square wave model.

From an analysis of Fig.4.14, it can also be added that, near the resonance frequency, the error that occurs using the analytical model with FHA is very low. On the other hand, moving far below the resonant frequency leads to a significant error, while above this smaller errors are reached. In conclusion, the evaluations obtained are consistent with what is present in the literature [12] [13].

4.3.2 Square Wave Model Working Points Map

Once an idea has been given of the error made with the FHA, also for this model a second simulation was carried out, to sweep more operating frequencies and operating gains. As was done in paragraph 4.2.2, the various load factors obtained are compared with the theoretical ones.

For the procedure to calculate the load factor and the phase shift of the second generator, refer to paragraph 4.2.2, where the calculation of the maximum gain at each operating frequency, by imposing the minimum possible load factor $Q = 0$, is still valid 4.6.

Given the considerations of the error committed in estimating the output resistance mostly at low frequencies, a good representation of the real model is expected from the simplified model.

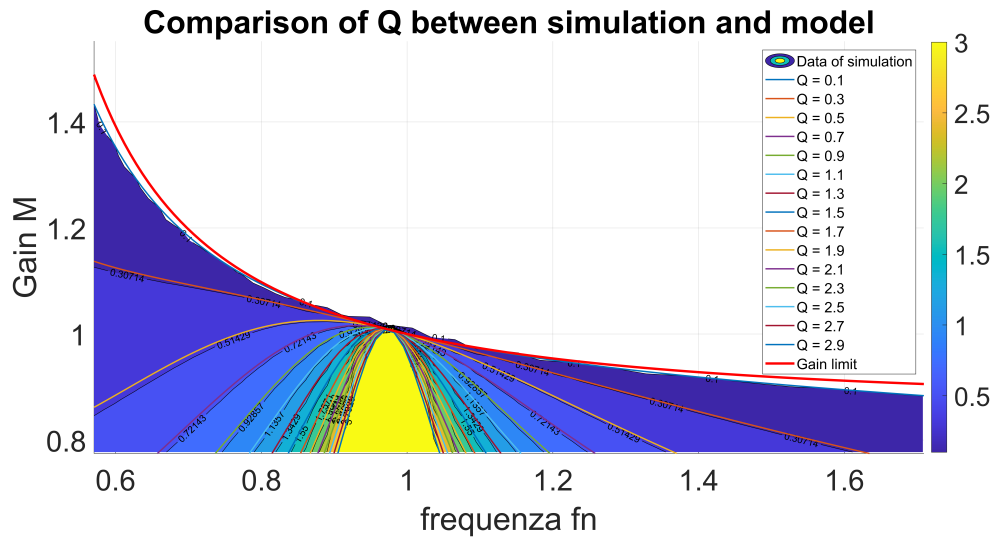


Figure 4.15: Comparison of voltage gain between the theoretical model and the obtained results in the square wave model.

For what concerns the gain at different frequencies and at different load factors Q , a good correspondence can be seen by comparing the results between Fig. 4.15 and Fig.4.8, in which all the curves seems to coincide.

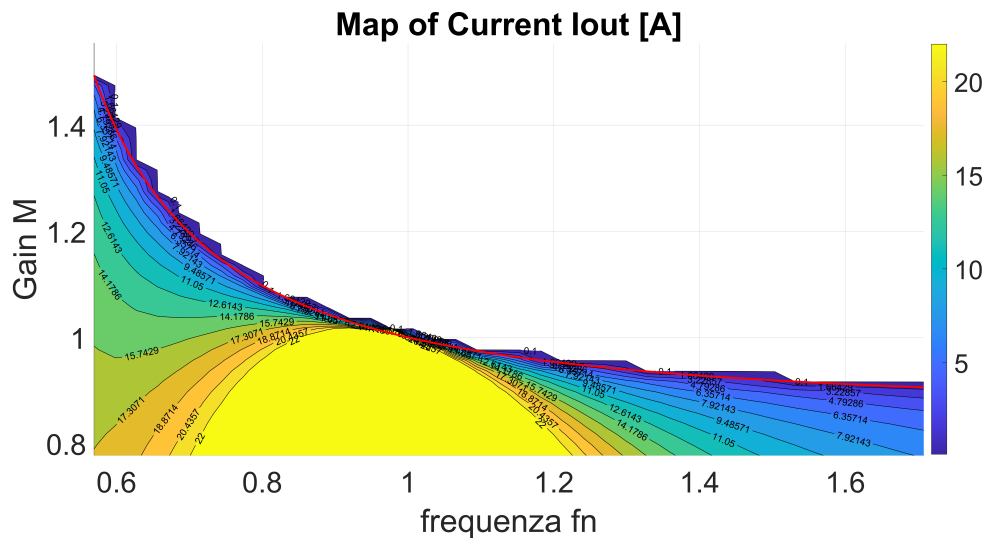


Figure 4.16: Output current map in the sinusoidal model.

In Fig.4.16 the currents absorbed by the equivalent output load for each operating

4.4. INVERTING AND RECTIFYING BRIDGE MODEL

point are mapped. By comparing this result with the one obtained in Fig.4.9 a difference can be seen. Indeed, at low frequency, the iso-lines doesn't match with each other perfectly.

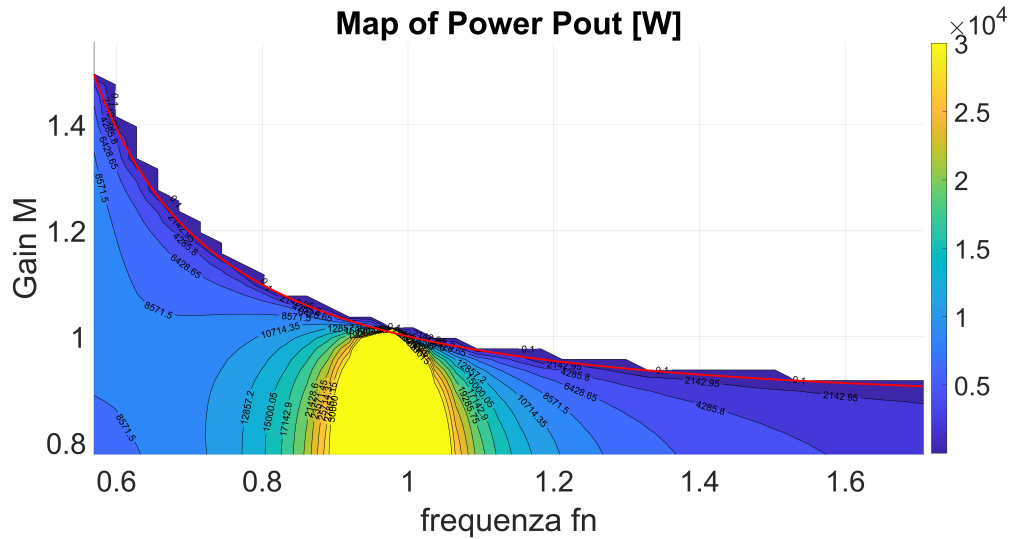


Figure 4.17: Output power map in the sinusoidal model.

Finally, the powers absorbed by the equivalent output load for each operating point are mapped in Fig.4.17. Here, the same consideration of the output current can be done by the comparison with 4.10.

4.4 Inverting and Rectifying Bridge Model

Before moving on to the full CLLC model, the following model is used to quickly check for correspondence with the previous square wave model.

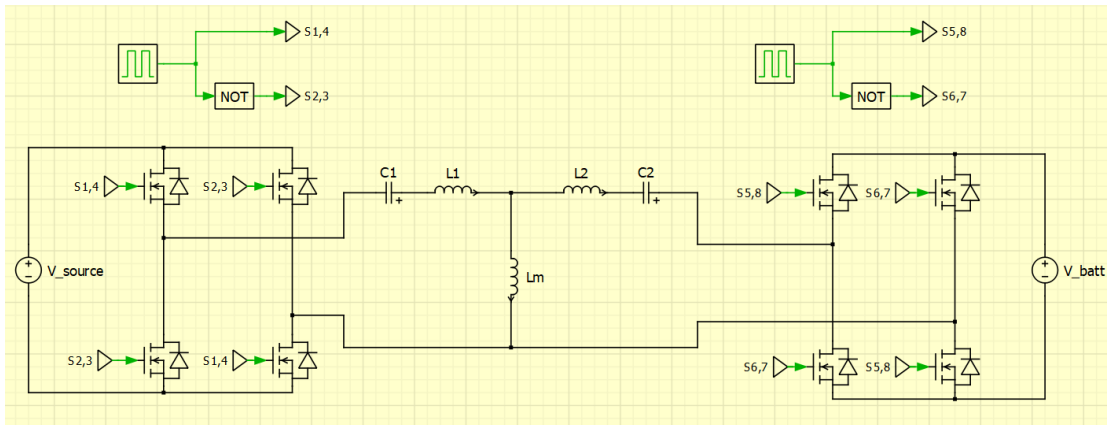


Figure 4.18: Inverting and rectifying bridge model.

4.4.1 Inverting and Rectifying Bridge Model Validation

The waveforms at the input of the rectifier bridge are the same as those obtained at the output of the square wave model. Therefore, utilizing these voltages and currents for output resistance calculation would yield identical results. However, with the introduction of the inverting and rectifying bridge, for greater consistency with theoretical considerations, opting for the voltages and currents at the output of the circuit, V_{bat} and I_{bat} , represents a better choice. These voltages and currents are still referred to the primary side, which means $V_{bat} = V'_{out}$ and $I_{bat} = I'_{out}$. Therefore, no carryover factor will appear in the calculation in Fig.4.19. Referring to the definition 3.12, the ratio $\frac{V'_{out}}{I'_{out}}$ is multiplied by a gain of $\frac{8}{\pi^2}$.

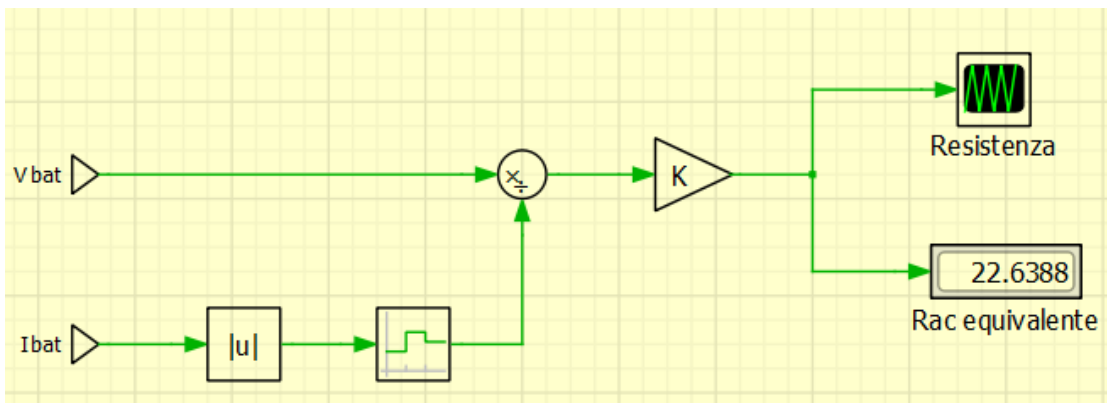


Figure 4.19: Calculation of equivalent output resistance in inverting and rectifying bridge model.

Running the simulation and testing the same resistance values of 4.3.1 at multiple

4.4. INVERTING AND RECTIFYING BRIDGE MODEL

operating frequencies, the results are shown in Fig.4.20, where the continuous lines are the obtained values from the model, while the dashed lines are the imposed values. From a comparison with Fig.4.13 obtained with the square wave model is possible to see how as the complexity of the model increases the error in the estimate also increases.

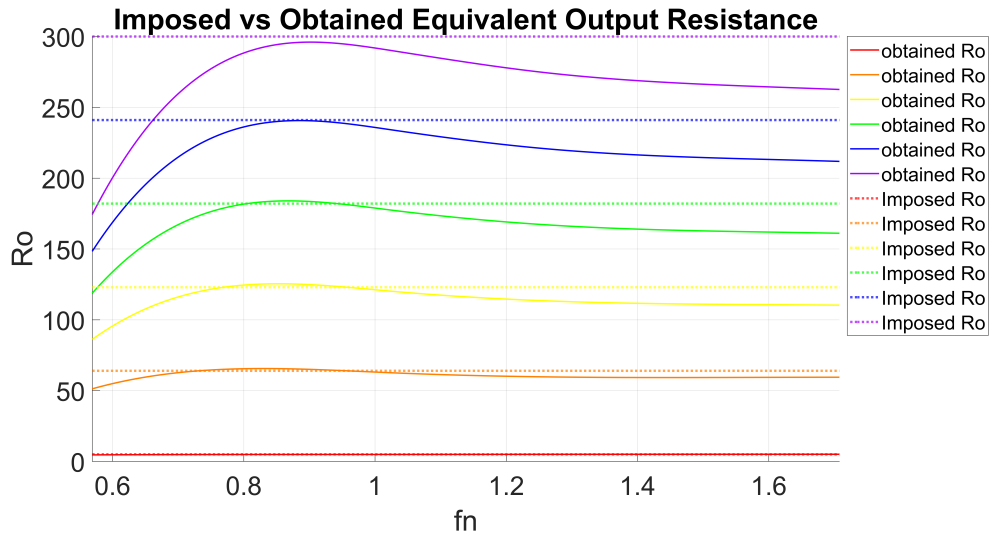


Figure 4.20: Comparison between the imposed and obtained equivalent output resistance in inverting and rectifying bridge model.

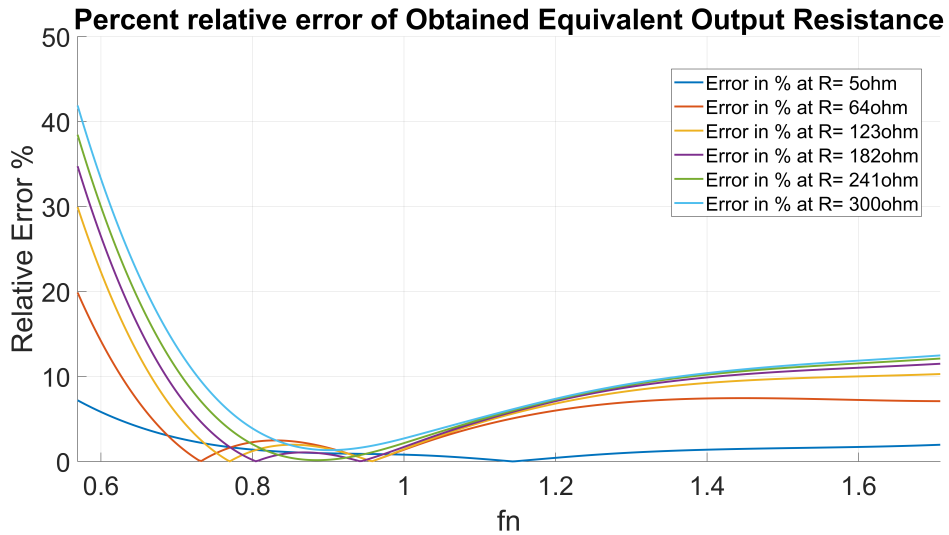


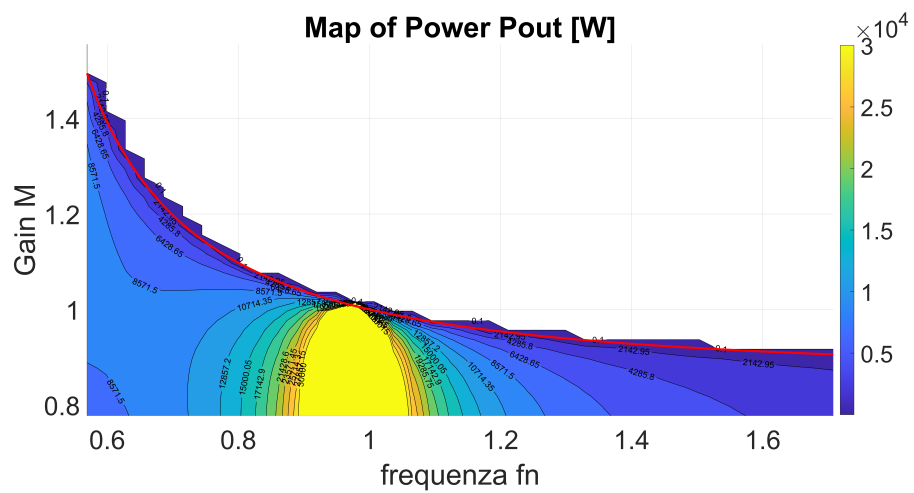
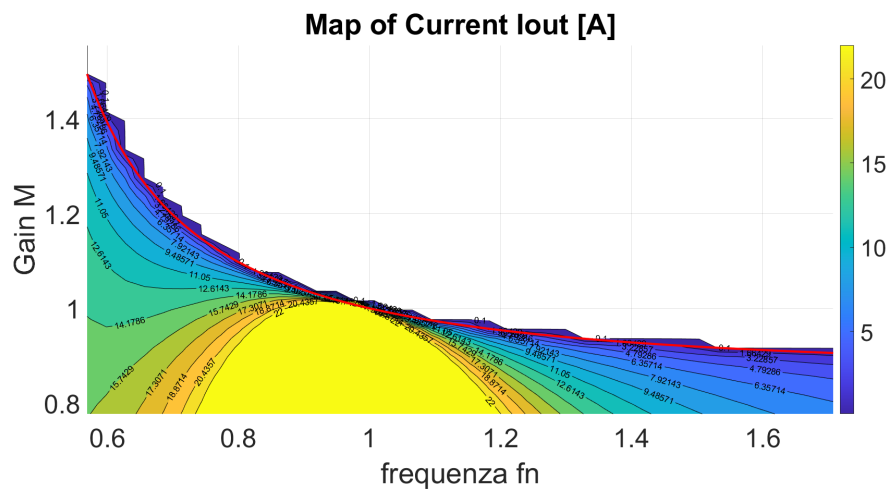
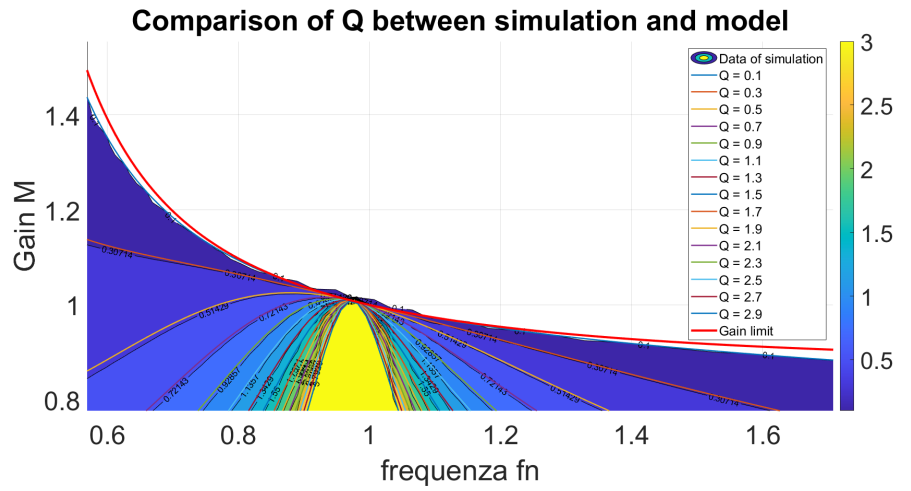
Figure 4.21: Relative percentage error between the imposed and obtained equivalent output resistance in inverting and rectifying bridge model.

To have an idea of what the error is, the relative percentage error is shown in Fig.4.21, in which in addition to presenting a significant error at low frequencies, modest inaccuracies also begin to appear at frequencies higher than the resonance frequency, without however exceeding 10% of the error.

4.4.2 Inverting and Rectifying Bridge Model Working Points Map

For continuity of reasoning, take a quick look at the current and power absorption of the output load.

4.4. INVERTING AND RECTIFYING BRIDGE MODEL



47
Figure 4.22

4.5 CLLC Resonant Converter Circuit

Lastly, the final complete model was achieved in Fig.4.23 without carrying over to the primary parameters of the resonant tank placed on the secondary of the transformer.

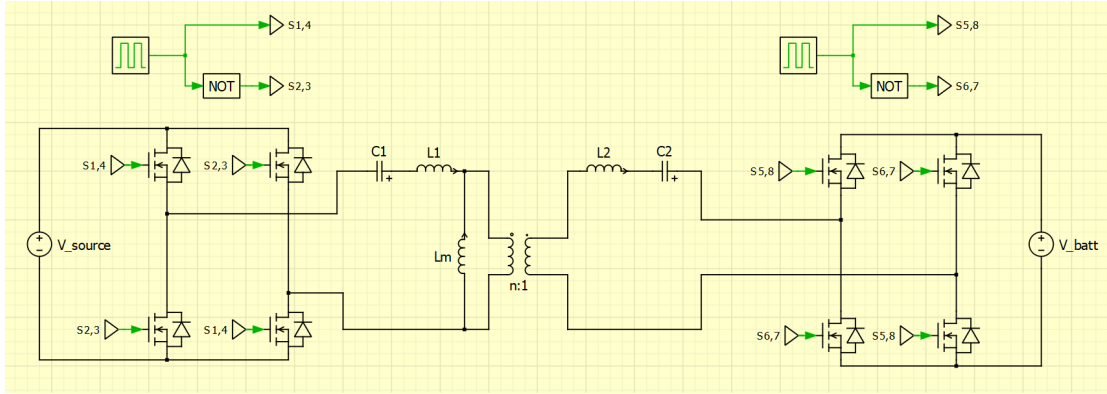


Figure 4.23: CLLC resonant converter schematic.

4.5.1 CLLC circuit Validation

To verify the model, the circuit's validation has to be done similarly to the previous simplified models. By applying the definition 3.12 in Fig.4.24, the ratio $\frac{V_{out}}{I_{out}}$ is multiplied by a gain of $\frac{8n_t^2}{\pi^2}$, where $V_{out} = V_{bat}$ and $I_{out} = I_{bat}$ are the battery voltage and the current through the battery.

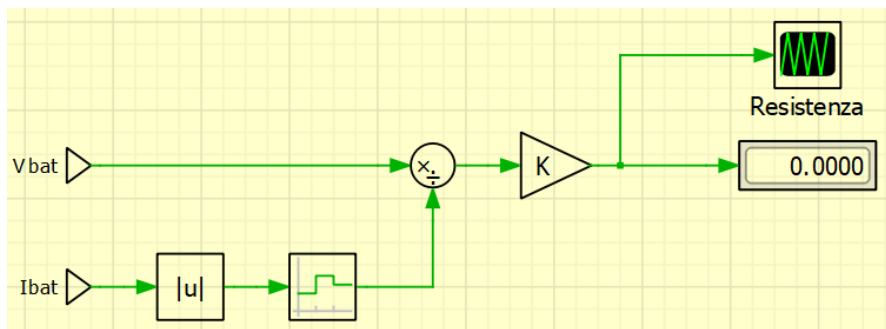
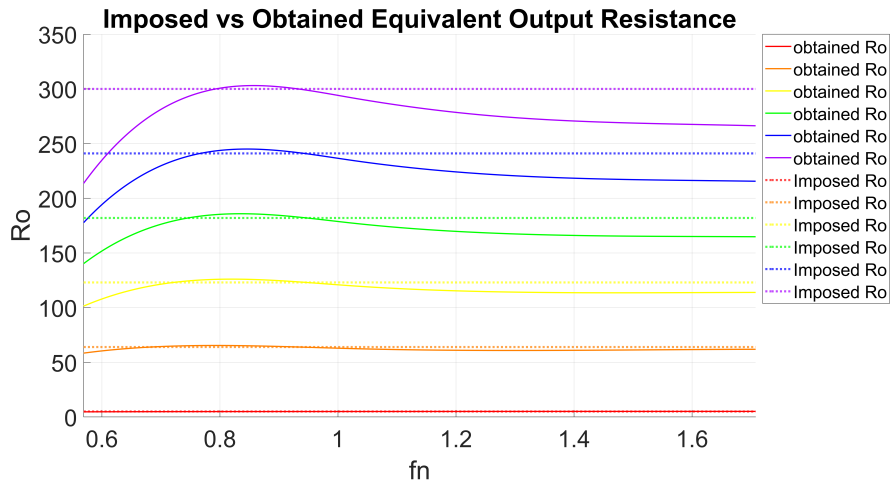


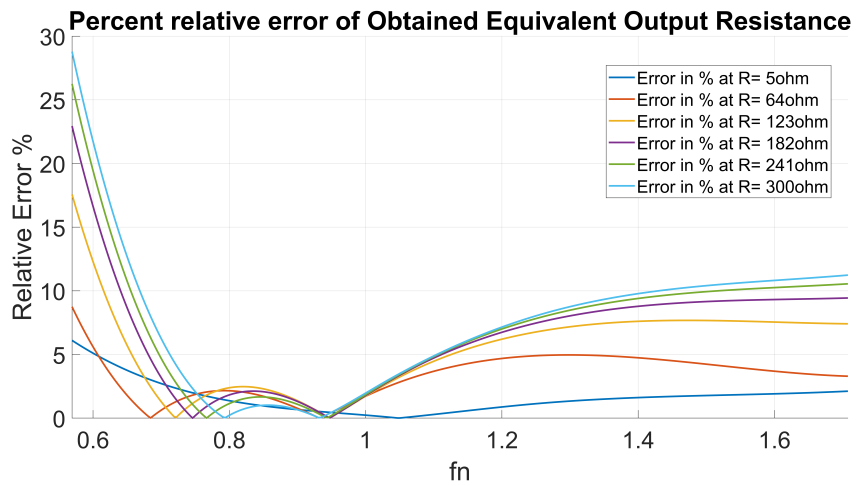
Figure 4.24: Calculation of equivalent output resistance in CLLC resonant converter schematic.

What is obtained are the same trends as the resistance calculation of the previous model in paragraph 4.4.1, shown in Fig.4.25, and so the same considerations can be done.

4.5. CLLC RESONANT CONVERTER CIRCUIT



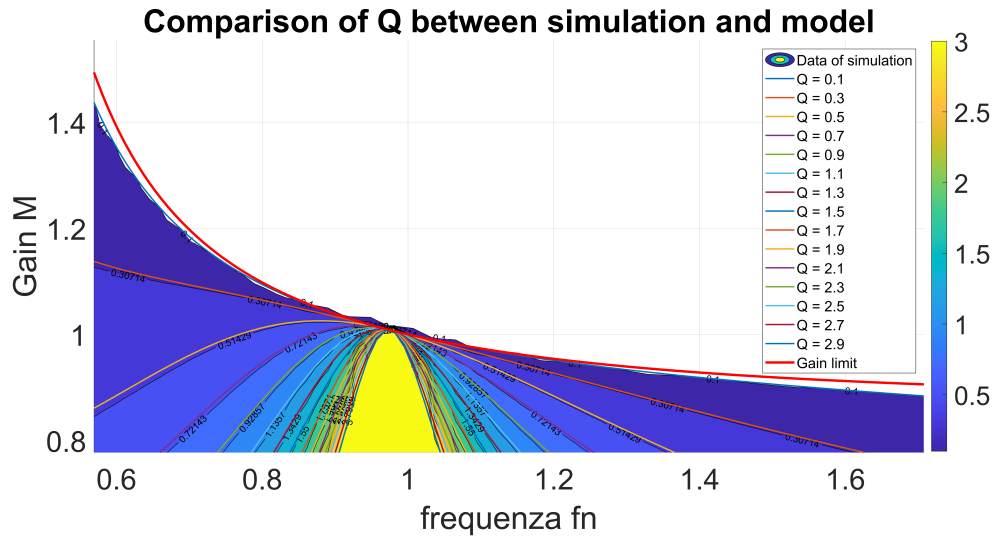
(a)



(b)

Figure 4.25: (a) comparison between imposed and obtained equivalent output resistance in CLLC scheme; (b) relative percentage error between the imposed and obtained equivalent output resistance in CLLC scheme.

4.5.2 CLLC circuit Working Points Map



CHAPTER 4. PLECS SIMULATIONS RESULTS

Chapter 5

Stresses Evaluation

The following chapter aims to analyze and evaluate what are the maximum stresses of the inductors and capacitors of the resonant tank, the transformer, and the MOSFETs. The fundamental values of interest for the sizing of the circuit elements are:

L_{R1}, L_{R2}, L_m	I_{RMS} I_{pk} V_{pk} ϕ
C_{R1}, C_{R2}	I_{RMS} V_{pk}
MOSFETs	I_{RMS} I_{pk}

Table 5.1: Quantities of interest for sizing.

The maps were obtained by making the converter work in several operating points and by recording the quantities shown in the table 5.1 for each element of interest. Then, by considering some limitations for operating regions the maps were elaborated to take the maximum stresses. The limitations that have been highlighted are the minimum and maximum gain and the gain limit to reach maximum power at most. This limit was obtained by seeing for which Q the maximum output power is obtained.

5.0.1 Primary Side Resonant Inductor Stresses

One of the main stresses of the resonant inductor of the primary side is the current RMS, necessary in the calculation of the conductor section. The maximum stress reached is shown in Fig.5.1, where a mask for the non-reachable regions is highlighted.

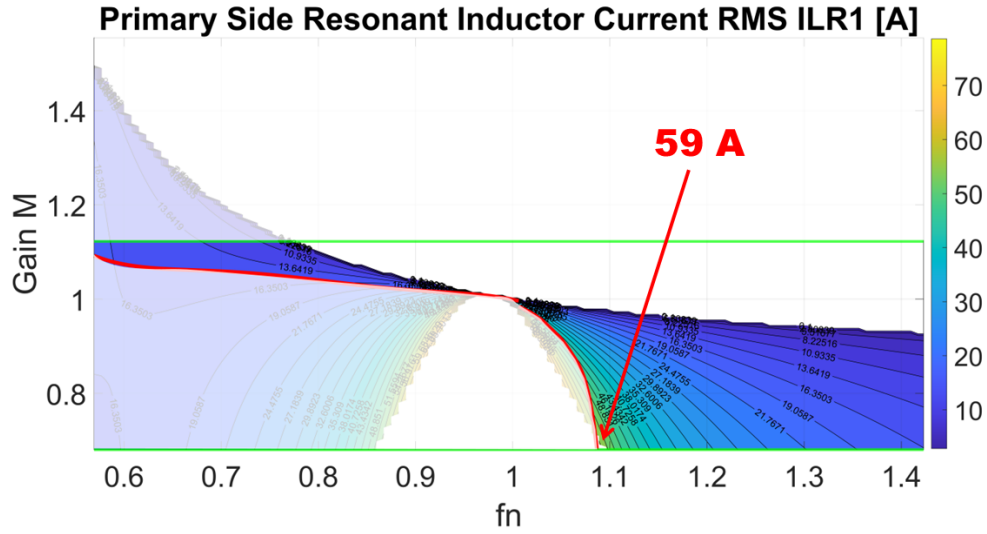


Figure 5.1: RMS current of primary resonant inductor.

Another stress of the resonant inductor of the primary side is the current peak value, necessary in the calculation of the saturation of the magnetic core. The maximum stress reached is shown in Fig.5.2, where a mask for the non-reachable regions is highlighted.

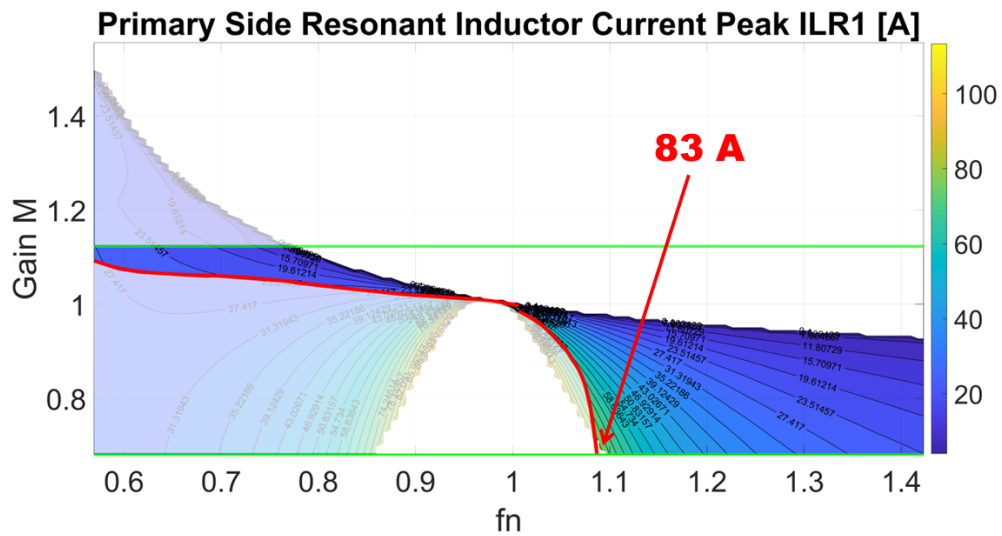


Figure 5.2: Peak current of primary resonant inductor.

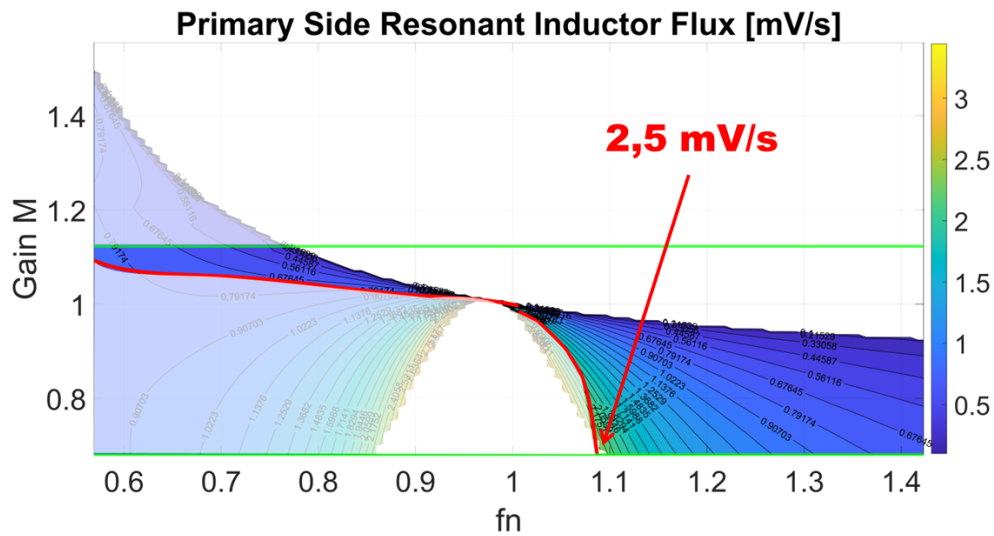
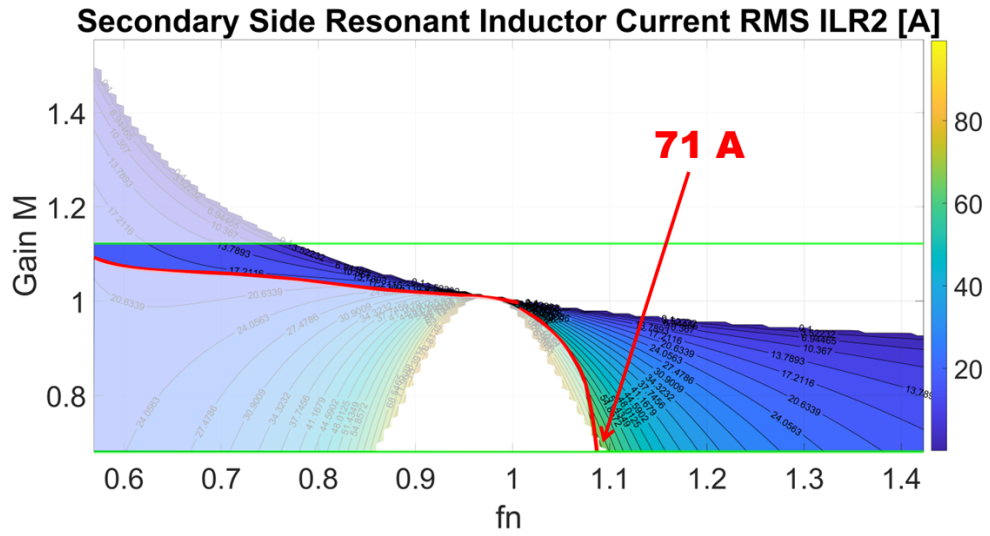


Figure 5.4: Maximum flux of primary resonant inductor.

5.0.2 Secondary Side Resonant Inductor Stresses

One of the main stresses of the resonant inductor of the secondary side is the current RMS, necessary in the calculation of the conductor section. The maximum stress reached is shown in Fig.5.5, where a mask for the non-reachable regions is highlighted.



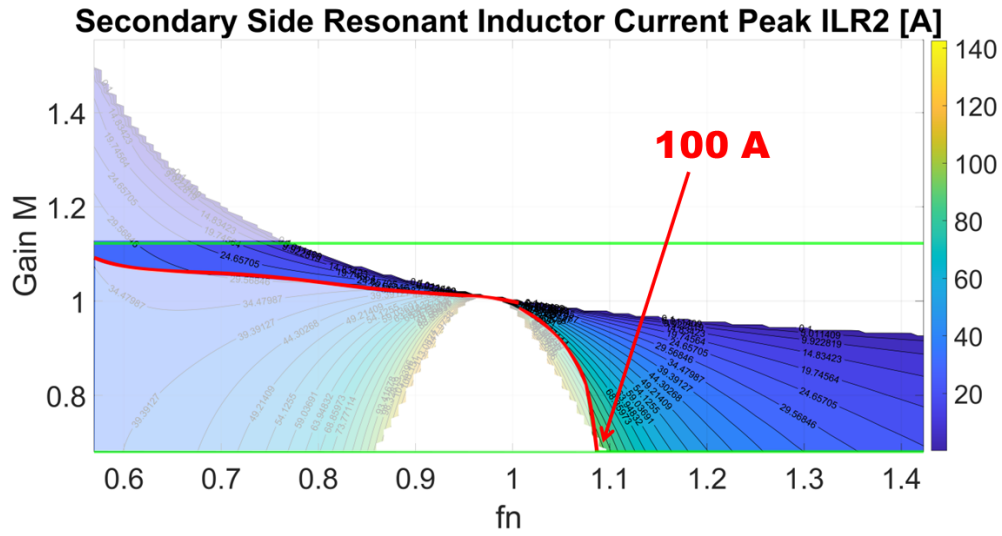


Figure 5.6: Peak current of secondary resonant inductor.

Then, the highest voltage attained by the resonant inductor on the secondary side is depicted in Fig.5.7, which is essential for calculating the electrical insulation of the conductor.

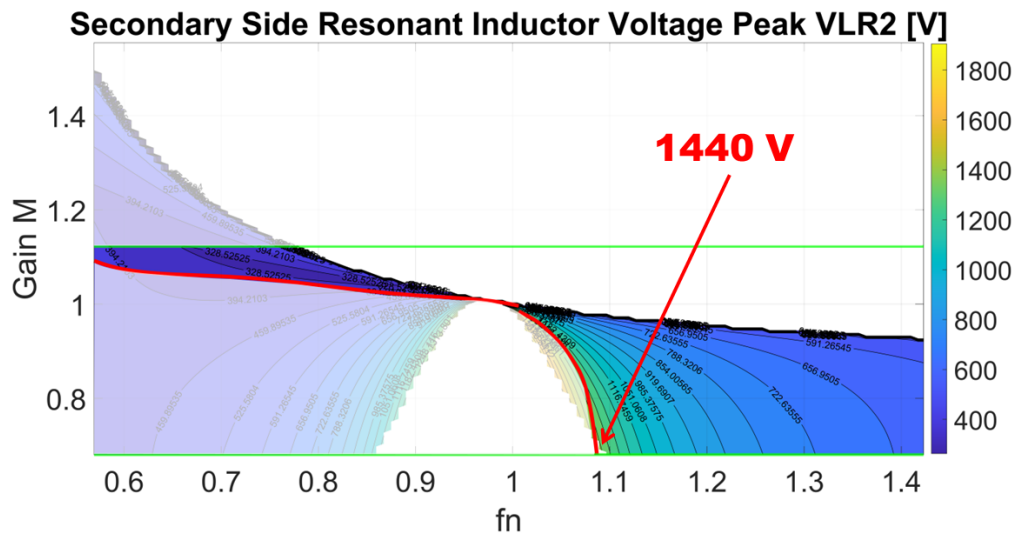


Figure 5.7: Peak voltage of secondary resonant inductor.

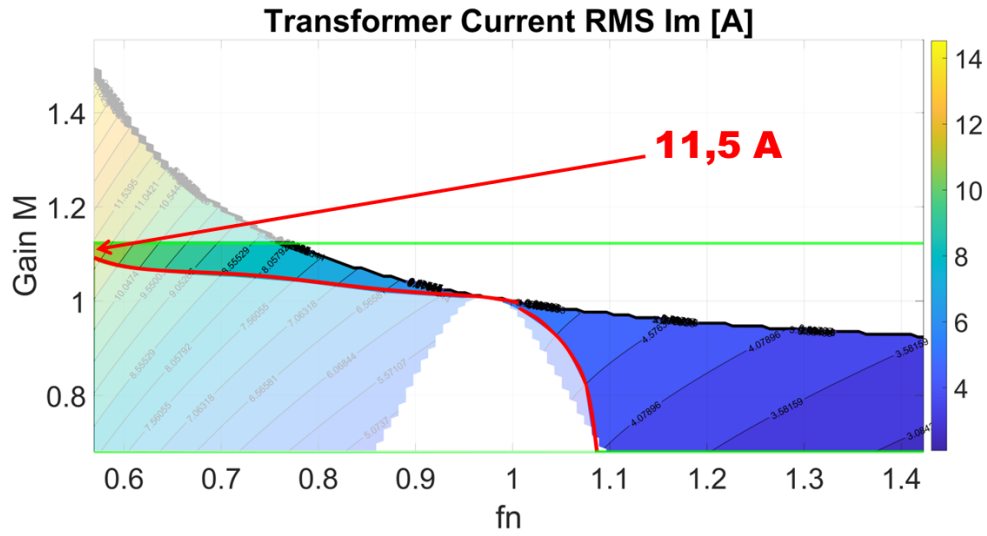


Figure 5.9: RMS current of transformer.

Another stress of the transformer is the current peak value, necessary in the calculation of the saturation of the magnetic core. The maximum stress reached is shown in Fig.5.10, where a mask for the non-reachable regions is highlighted.

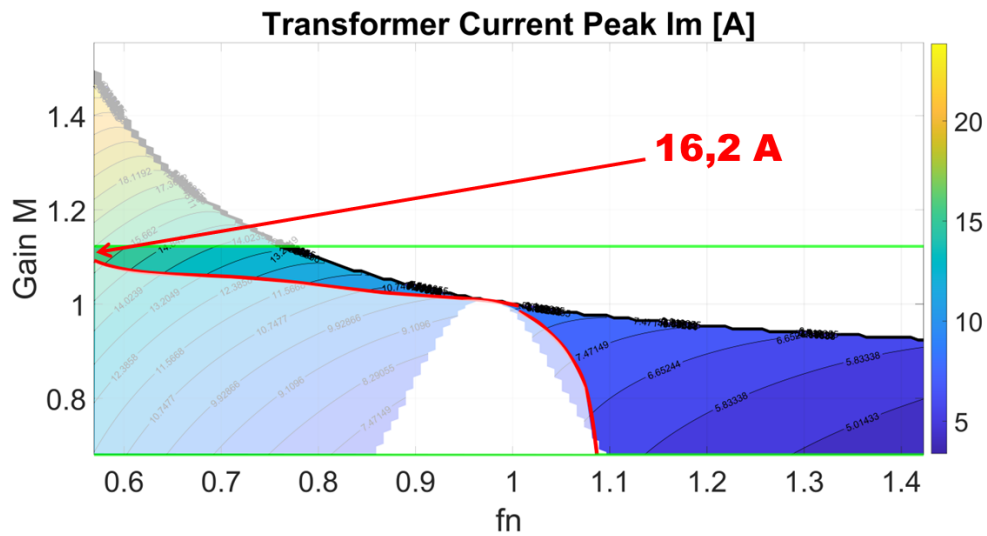


Figure 5.10: Peak current of transformer.

The maximum voltage reached by the transformer is shown in Fig.5.11, necessary in the calculation of the conductor's electrical insulation.

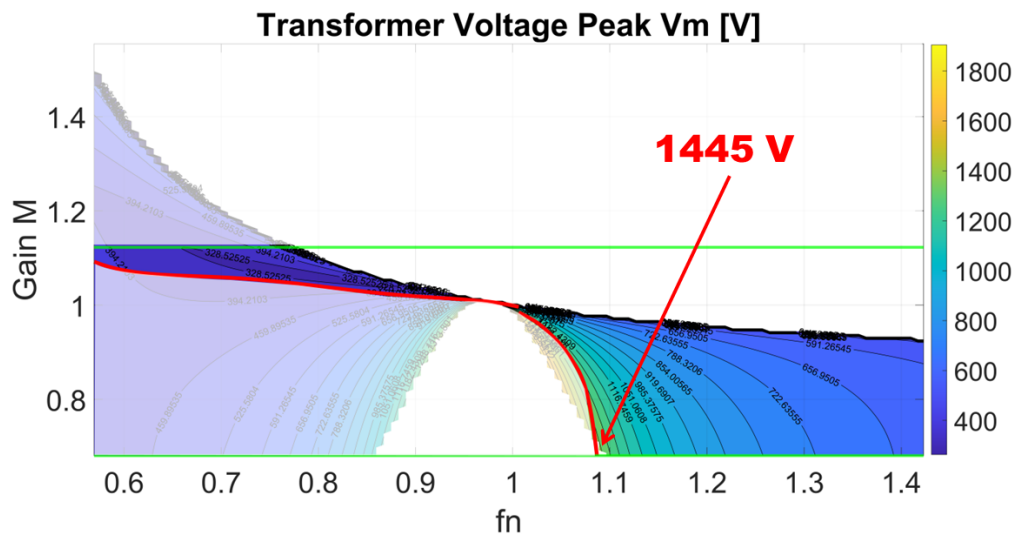


Figure 5.11: Peak voltage of transformer.

Finally, the maximum flux achieved by the transformer is presented in Fig.5.12. This value is crucial for determining the magnetic core's cross-sectional area in calculations.

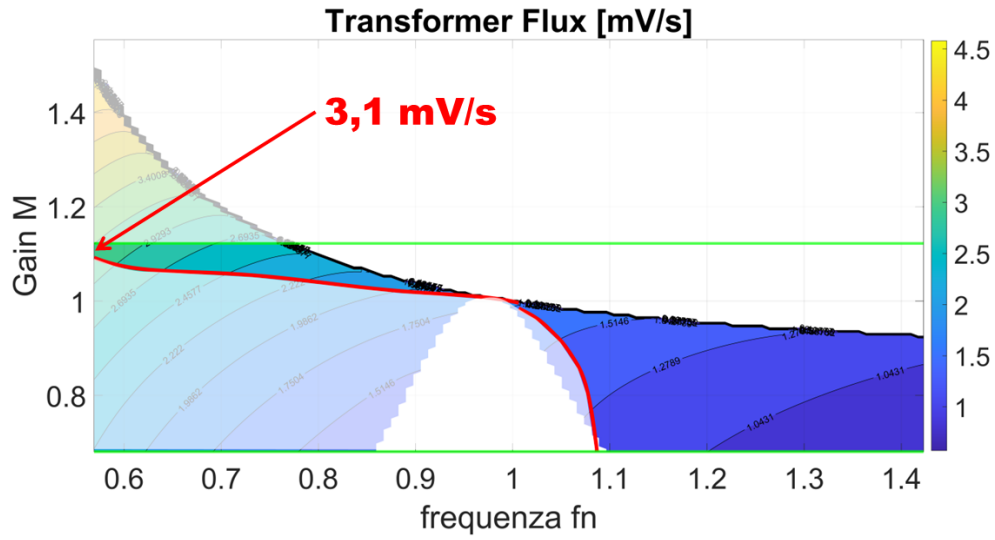


Figure 5.12: Maximum flux of transformer.

5.0.4 Primary Side Resonant Capacitor Stresses

The stresses of the resonant capacitor of the primary side are reported in Fig.5.13, taking the maximum stresses within the operating regions highlighted with a mask.

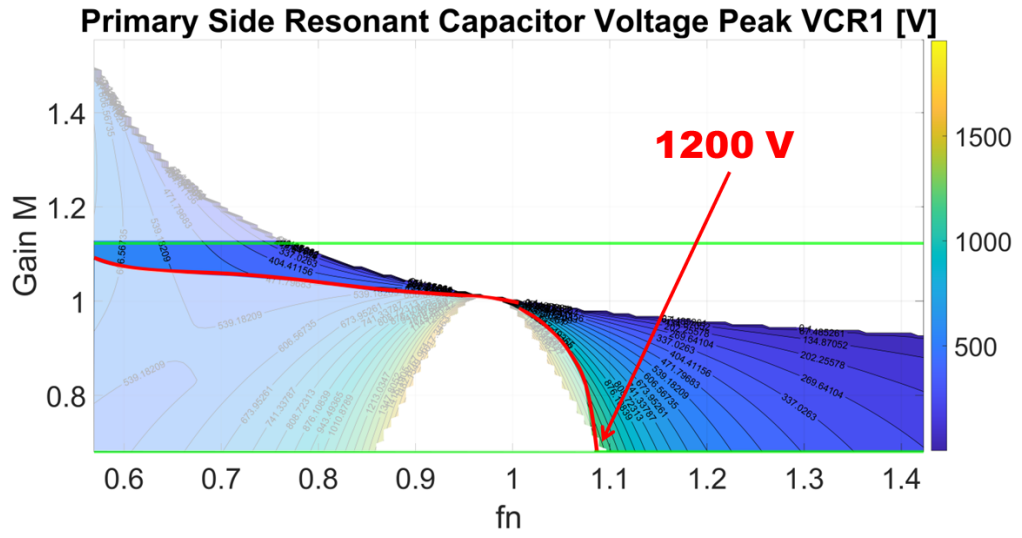
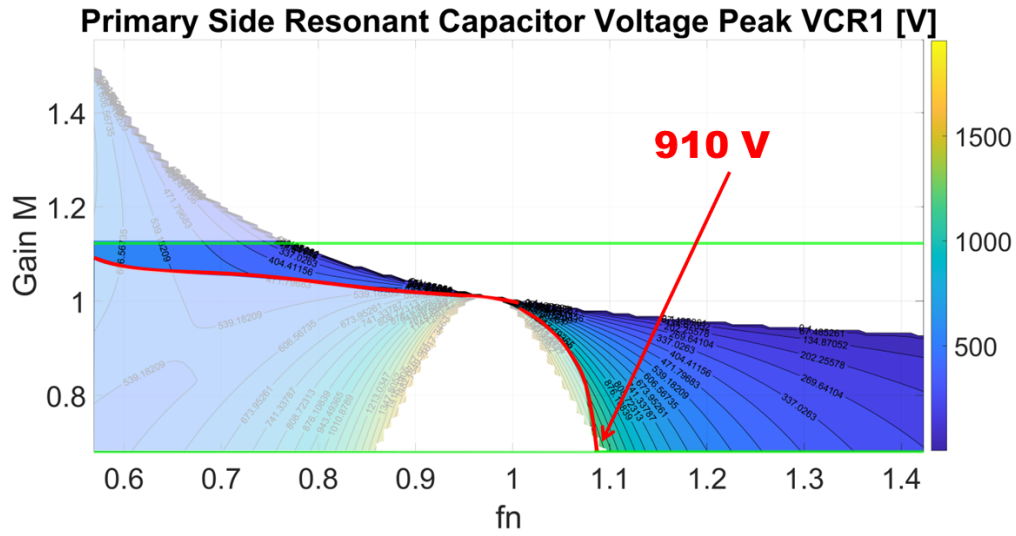


Figure 5.13: Peak voltage of primary side capacitor.

5.0.5 Primary Side Resonant Capacitor Stresses

The stresses of the resonant capacitor of the secondary side are reported in Fig.5.14, taking the maximum stresses within the operating regions.



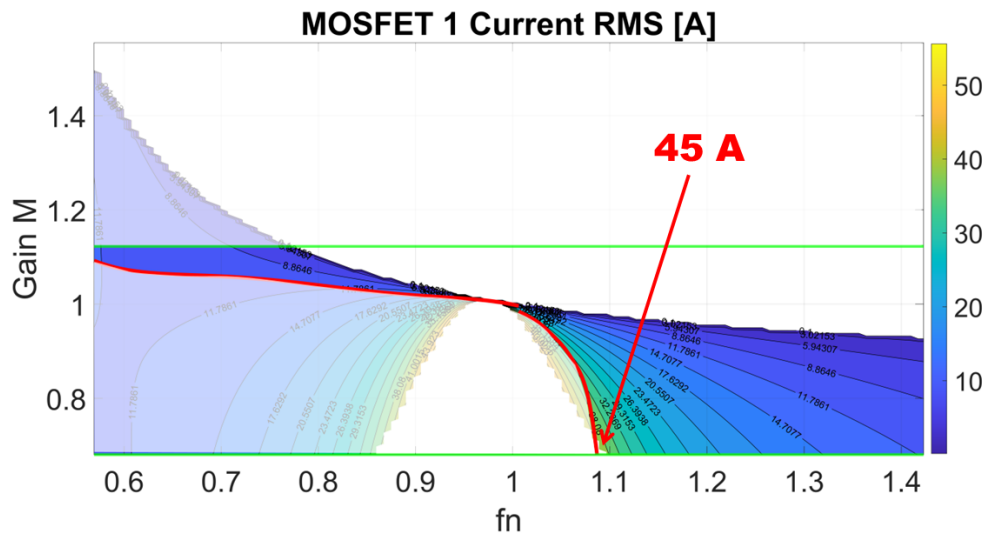


Figure 5.15: MOSFET 1 RMS current.

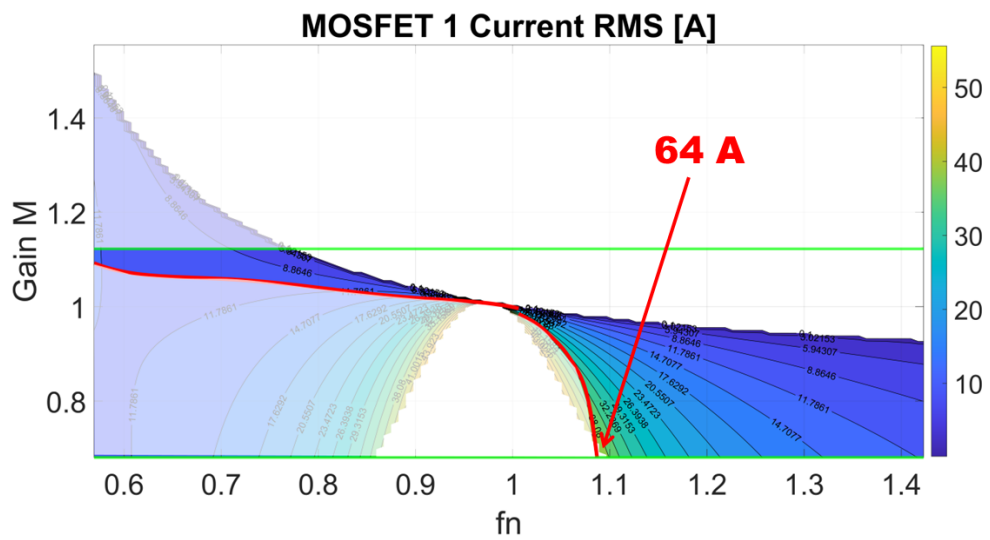


Figure 5.16: MOSFET 1 peak current.

Then, the stresses of one of the MOSFETs of the rectifier bridge are reported below, where the RMS and peak current are shown respectively in Fig.5.17 and in Fig.5.18.

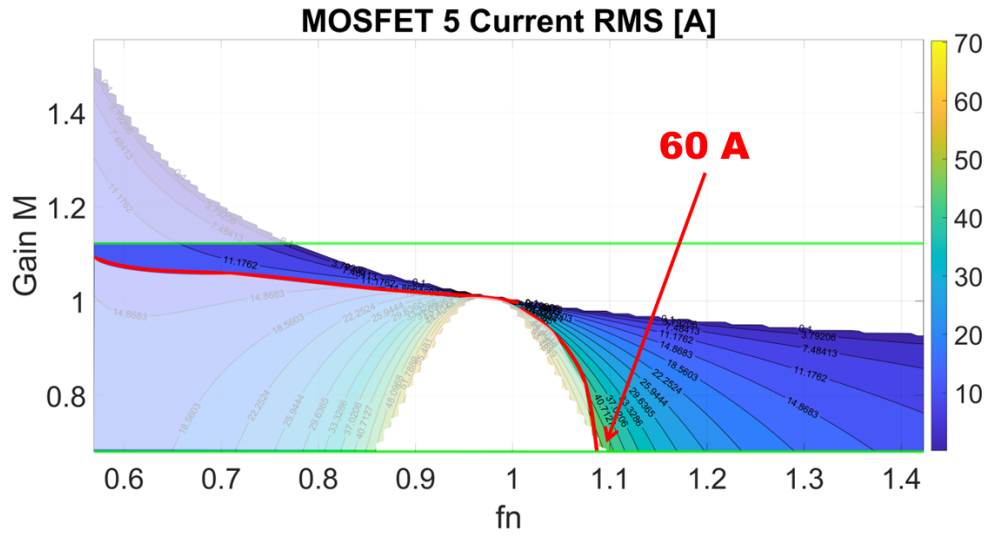


Figure 5.17: MOSFET 5 RMS current.

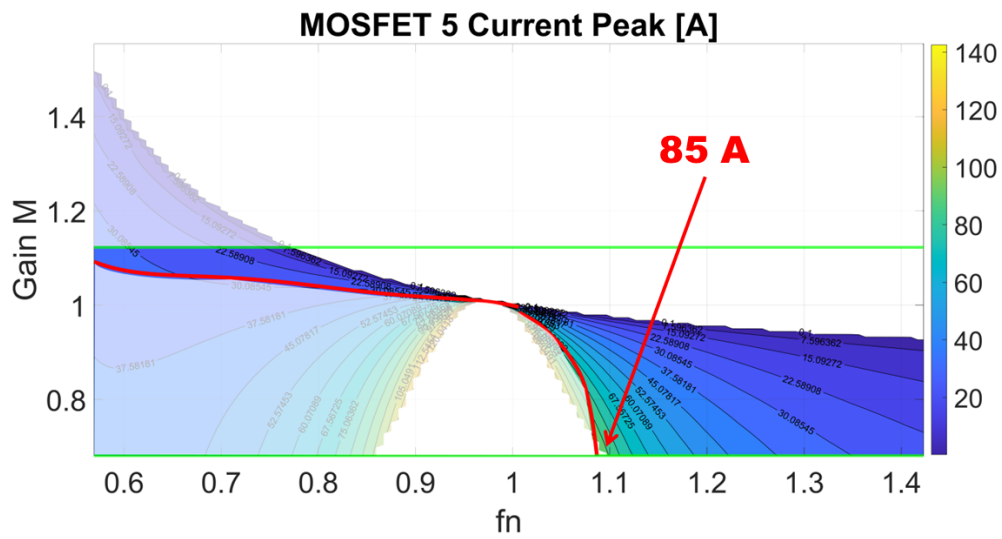


Figure 5.18: MOSFET 5 peak current.

Chapter 6

Conclusions and Future Works

6.1 Conclusions

From the observations made, the results of this thesis work can be highlighted as follows:

- Based on the analysis conducted, the mathematical calculation of the phase shift could be considered satisfying because reflects the frequency behaviour of the current at the secondary side. To support this statement, a comparison between the trends of the analytical development and the trends obtained in the simulation on LTspiceXVII has been done where good correspondence has been noticed. Additionally, a basic circuit simulation was conducted using PLECS, consisting of a resistor at the output. It was observed that the phase shift formula accurately reflects the phase difference between the current flowing through the resistor and the input generator voltage. With negligible discrepancies, such as 0.18° at significantly higher frequencies, approximately 2.5 times greater than the resonant frequency, the reliability of the phase shift formula has been affirmed. Then, this formula is unequivocally utilized to control the opening and closing of the rectifier bridge switches, ensuring synchronous rectification.
- In addition to the aforementioned findings, an evaluation of the validity of the treated method with the use of FHA has been done. For high output equivalent resistance, the FHA makes estimation errors at a frequency far away from the resonant frequency. This result can be used to stay close to the resonant frequency when a high load is required by the application. In essence, the simplified circuit effectively mirrors the converter when operating within proximity to its resonance frequency, enabling a comprehensive study of its frequency behavior. On the other hand, it is difficult to have a wide range of operating frequencies. Hence, focusing on phenomena between 0.7 times and 1.3 times the resonance frequency provides a

suitable range where assumptions and hypotheses do not undermine the accuracy of the results.

- Moreover, the simulation tool employed for analyzing point-by-point stresses is robust and valuable, as it captures all stresses at different operating conditions, providing a comprehensive framework for future design assessments.

6.2 Future Works

Considering the perspective of Prima Electro, the company where the thesis work was carried out, the objective of developing a 25 kW resonant CLLC prototype capable of providing a wide spectrum of output voltages is underway. Consequently, exploiting the results derived from this thesis work becomes fundamental to shape an effective design process, establish robust control mechanisms, and conduct laboratory tests to validate the simulated results. This approach provides a solid foundation for prototype development and optimization, aligning with the company's goals and driving advancements in resonant power converter technology.

Appendix A

Calculation Gain Formula in Forward Mode

Referring to the unified equivalent circuit depicted in Fig. A.1 in forward mode, to simplify the notations are defined:

$$Z_1 = j\omega_s L_{R1} + \frac{1}{j\omega_s C_{R1}} \quad (\text{A.1})$$

$$Z_2 = j\omega_s L'_{R2} + \frac{1}{j\omega_s C'_{R2}} \quad (\text{A.2})$$

$$Z_m = j\omega_s L_m \quad (\text{A.3})$$

where:

$$L_{R1} = L_{s,R1} ; L'_{R2} = L'_{s,R2} ; L_m = L_{s,m} ; C_{R1} = C_{s,R1} ; C'_{R2} = C'_{s,R2} ; R'_o = R'_{o,FB,FHA}$$

APPENDIX A. CALCULATION GAIN FORMULA IN FORWARD MODE

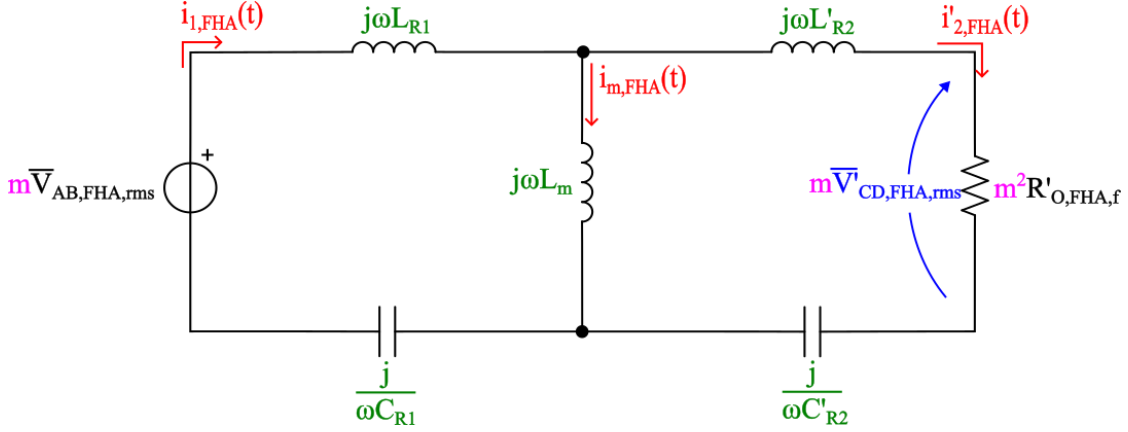


Figure A.1: Equivalent circuit of SFBCLLC in forward mode.

The parameters of the equivalent circuit are all the parameters referred to the primary of the transformer. This means that L_{R1} , C_{R1} and L_m remain unchanged because they are already referred to the primary, while L_{R2} , C_{R2} and the output resistance must be reported considering the turns ratio: $L'_{R2} = n_t^2 L_{R2}$; $C'_{R2} = \frac{C_{R2}}{n_t^2}$; $R'_o = \frac{8n_t^2}{\pi^2} R_{out,DC}$.

The transfer function is:

$$\begin{aligned}
 H_F(j\omega, Q) &= \frac{Z_m \parallel (Z_2 + R'_o)}{Z_1 + Z_m \parallel (Z_2 + R'_o)} \frac{R'_o}{Z_2 + R'_o} = \frac{\frac{Z_m(Z_2 + R'_o)}{Z_m + Z_2 + R'_o}}{Z_1 + \frac{Z_m(Z_2 + R'_o)}{Z_m + Z_2 + R'_o}} \frac{R'_o}{Z_2 + R'_o} = \\
 &= \frac{Z_m R'_o}{Z_m Z_1 + Z_1 Z_2 + Z_1 R'_o + Z_m Z_2 + Z_m R'_o} = \frac{1}{\frac{Z_1}{R'_o} + \frac{Z_1 Z_2}{Z_m R'_o} + \frac{Z_1}{Z_m} + \frac{Z_2}{R'_o} + 1} = \quad (A.4) \\
 &= \frac{1}{\frac{Z_1}{R'_o} + \frac{Z_1}{Z_m} \left(\frac{Z_2}{R'_o} + 1 \right) + \frac{Z_2}{R'_o} + 1}
 \end{aligned}$$

Let's introduce the following parameters, by considering that $\omega_{R1} = \frac{1}{\sqrt{L_{R1} C_{R1}}}$

$$k = \frac{L_m}{L_{R1}} \quad (A.5)$$

$$Q = \frac{\sqrt{\frac{L_{R1}}{C_{R1}}}}{R'_o} \quad (A.6)$$

$$\omega_n = \frac{\omega_s}{\omega_{R1}} \quad (A.7)$$

$$a = \frac{L'_{R2}}{L_{R1}} \quad (A.8)$$

$$b = \frac{C'_{R2}}{C_{R1}} \quad (\text{A.9})$$

Going to analyze some elements of the equation A.4, it's possible to obtain A.10, A.11 and A.12:

$$\begin{aligned} \frac{Z_1}{R'_o} &= \frac{j\omega_s L_{R1}}{R'_o} + \frac{1}{j\omega_s C_{R1} R'_o} = j\omega_n \frac{L_{R1}}{\sqrt{L_{R1} C_{R1}}} \frac{1}{R'_o} + \frac{1}{j\omega_n \frac{C_{R1}}{\sqrt{L_{R1} C_{R1}}} R'_o} = \\ &= j\omega_n \frac{\sqrt{\frac{L_{R1}}{C_{R1}}}}{R'_o} - \frac{j}{\omega_n \frac{R'_o}{\sqrt{\frac{L_{R1}}{C_{R1}}}}} = j\omega_n Q - j \frac{Q}{\omega_n} = jQ \left(\omega_n - \frac{1}{\omega_n} \right) \end{aligned} \quad (\text{A.10})$$

Next:

$$\begin{aligned} \frac{Z_1}{Z_m} &= \frac{j\omega_s L_{R1}}{j\omega_s L_m} + \frac{1}{j\omega_s C_{R1}} \frac{1}{j\omega_s L_m} = \frac{L_{R1}}{L_m} + \frac{1}{j^2 \omega_s^2 C_{R1} L_m} = \\ &= \frac{1}{k} - \frac{1}{\omega_n^2 \frac{1}{L_{R1} C_{R1}} C_{R1} k L_{R1}} = \frac{1}{k} - \frac{1}{\omega_n^2 k} \end{aligned} \quad (\text{A.11})$$

And finally:

$$\begin{aligned} \frac{Z_2}{R'_o} &= \frac{j\omega_s L'_{R2} + \frac{1}{j\omega_s C'_{R2}}}{R'_o} = \frac{j\omega_s L'_{R2}}{R'_o} + \frac{1}{j\omega_s C'_{R2} R'_o} = \\ &= j\omega_n \frac{1}{\sqrt{L_{R1} C_{R1}}} \frac{L'_{R2}}{R'_o} + \frac{1}{j\omega_n \frac{1}{\sqrt{L_{R1} C_{R1}}} C'_{R2} R'_o} = \\ &= j\omega \frac{a L_{R1}}{\sqrt{L_{R1} C_{R1}}} \frac{1}{R'_o} + \frac{1}{j\omega_n \frac{b C_{R1}}{\sqrt{L_{R1} C_{R1}}} R'_o} = \\ &= j\omega_n a \frac{\sqrt{\frac{L_{R1}}{C_{R1}}}}{R'_o} + \frac{1}{j\omega_n b \frac{R'_o}{\sqrt{\frac{L_{R1}}{C_{R1}}}}} = j\omega_n a Q - \frac{jQ}{\omega_n b} = \\ &= jQ \left(a\omega_n - \frac{1}{b\omega_n} \right) \end{aligned} \quad (\text{A.12})$$

APPENDIX A. CALCULATION GAIN FORMULA IN FORWARD MODE

Replacing in the transfer function A.4:

$$\begin{aligned}
 H(j\omega_n, Q) &= \frac{1}{jQ(\omega_n - \frac{1}{\omega_n}) + (\frac{1}{k} - \frac{1}{\omega_n^2 k}) \left[jQ(a\omega_n - \frac{1}{b\omega_n}) + 1 \right] + jQ(a\omega_n - \frac{1}{b\omega_n}) + 1} = \\
 &= \frac{1}{jQ(\omega_n - \frac{1}{\omega_n}) + (\frac{1}{k} - \frac{1}{\omega_n^2 k}) \left[jQ(a\omega_n - \frac{1}{b\omega_n}) \right] + (\frac{1}{k} - \frac{1}{\omega_n^2 k}) + jQ(a\omega_n - \frac{1}{b\omega_n}) + 1} = \\
 &= \frac{1}{\left(\frac{1}{k} - \frac{1}{\omega_n^2 k} + 1 \right) + jQ \left(\omega_n - \frac{1}{\omega_n} \right) + jQ \left(\frac{a\omega_n}{k} - \frac{1}{kb\omega_n} - \frac{a}{k\omega_n} + \frac{1}{kb\omega_n^3} \right) + jQ \left(a\omega_n - \frac{1}{b\omega_n} \right)}
 \end{aligned} \tag{A.13}$$

The final formula is:

$$H(j\omega_n, Q) = \frac{1}{\left(\frac{1}{k} - \frac{1}{\omega_n^2 k} + 1 \right) + j \left[Q\omega_n \left(1 + \frac{a}{k} + a \right) - \frac{Q}{\omega_n} \left(\frac{1}{kb} + \frac{a}{k} + \frac{1}{b} + 1 \right) + \frac{Q}{kb\omega_n^3} \right]} \tag{A.14}$$

The module of A.14 is calculated in A.15:

$$M(j\omega_n, Q) = \left\{ \left(\frac{1}{k} - \frac{1}{\omega_n^2 k} + 1 \right)^2 + \left[Q\omega_n \left(1 + \frac{a}{k} + a \right) - \frac{Q}{\omega_n} \left(\frac{1}{kb} + \frac{a}{k} + \frac{1}{b} + 1 \right) + \frac{Q}{kb\omega_n^3} \right]^2 \right\}^{-\frac{1}{2}} \tag{A.15}$$

Appendix B

Calculation Gain Formula in Reverse Mode

Referring to the unified equivalent circuit depicted in Fig. B.1 in reverse mode, to simplify the notations are defined:

$$Z_1 = j\omega_s L_{R2} + \frac{1}{j\omega_s C_{R2}} \quad (\text{B.1})$$

$$Z_2 = j\omega_s L''_{R1} + \frac{1}{j\omega_s C''_{R1}} \quad (\text{B.2})$$

$$Z_m = j\omega_s L''_m \quad (\text{B.3})$$

where:

$$L''_{R1} = L''_{s,R1} ; L_{R2} = L_{s,R2} ; L''_m = L''_{s,m} ; C''_{R1} = C''_{s,R1} ; C_{R2} = C_{s,R2} ; R''_o = R''_{o,FB,FHA}$$

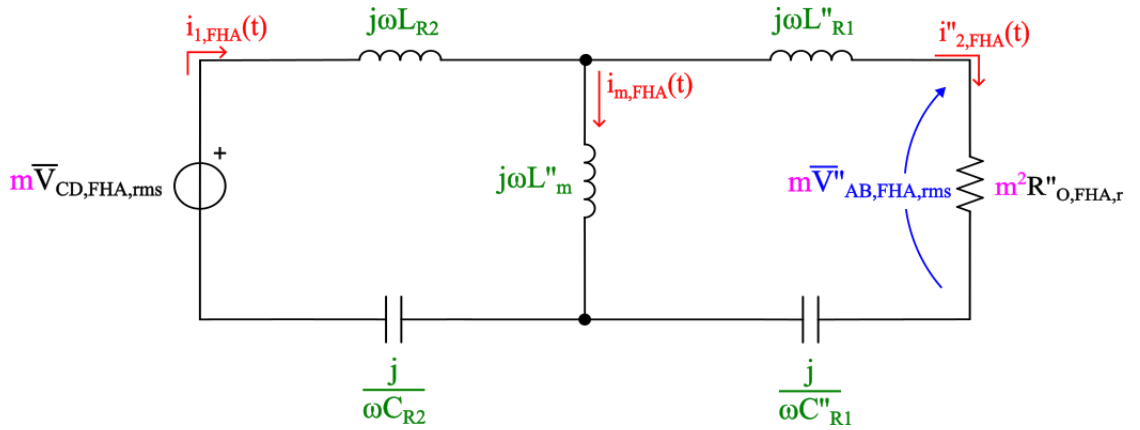


Figure B.1: Equivalent circuit of in reverse mode.

APPENDIX B. CALCULATION GAIN FORMULA IN REVERSE MODE

The parameters of the equivalent circuit are all the parameters referred to the secondary of the transformer. This means that L_{R2} , C_{R2} remain unchanged because they are already referred to the secondary, while L_{R1} , C_{R1} , L_m and the equivalent output resistance must be reported considering the turns ratio: $L''_{R1} = \frac{L_{R1}}{n_t^2}$; $C''_{R1} = n_t^2 C_{R1}$; $R''_o = \frac{8}{n_t^2 \pi^2} R_{out,DC}$.

The transfer function is:

$$\begin{aligned} H_F(j\omega, Q) &= \frac{Z_m \parallel (Z_2 + R''_o)}{Z_1 + Z_m \parallel (Z_2 + R''_o)} \frac{R''_o}{Z_2 + R''_o} = \frac{\frac{Z_m(Z_2 + R''_o)}{Z_m + Z_2 + R''_o}}{Z_1 + \frac{Z_m(Z_2 + R''_o)}{Z_m + Z_2 + R''_o}} \frac{R''_o}{Z_2 + R''_o} = \\ &= \frac{Z_m R''_o}{Z_m Z_1 + Z_1 Z_2 + Z_1 R''_o + Z_m Z_2 + Z_m R''_o} = \frac{1}{\frac{Z_1}{R''_o} + \frac{Z_1 Z_2}{Z_m R''_o} + \frac{Z_1}{Z_m} + \frac{Z_2}{R''_o} + 1} = \text{(B.4)} \\ &= \frac{1}{\frac{Z_1}{R''_o} + \frac{Z_1}{Z_m} \left(\frac{Z_2}{R''_o} + 1 \right) + \frac{Z_2}{R''_o} + 1} \end{aligned}$$

Let's introduce the following parameters, by considering that $\omega_{R1} = \frac{1}{\sqrt{L_{R2} C_{R2}}}$

$$k = \frac{L''_m}{L_{R2}} \quad \text{(B.5)}$$

$$Q = \frac{\sqrt{\frac{L_{R2}}{C_{R2}}}}{R''_o} \quad \text{(B.6)}$$

$$\omega_n = \frac{\omega_s}{\omega_{R1}} \quad \text{(B.7)}$$

$$a = \frac{L''_{R1}}{L_{R2}} \quad \text{(B.8)}$$

$$b = \frac{C''_{R1}}{C_{R2}} \quad \text{(B.9)}$$

Going to analyze some elements of the equation B.4, it's possible to obtain B.10, B.11 and B.12:

$$\begin{aligned} \frac{Z_1}{R''_o} &= \frac{j\omega_s L_{R2}}{R''_o} + \frac{1}{j\omega_s C_{R2} R''_o} = j\omega_n \frac{L_{R2}}{\sqrt{L_{R2} C_{R2}}} \frac{1}{R''_o} + \frac{1}{j\omega_n \frac{C_{R2}}{\sqrt{L_{R2} C_{R2}}} R''_o} = \\ &= j\omega_n \frac{\sqrt{\frac{L_{R2}}{C_{R2}}}}{R''_o} - \frac{j}{\omega_n \frac{R''_o}{\sqrt{\frac{L_{R2}}{C_{R2}}}}} = j\omega_n Q - j \frac{Q}{\omega_n} = jQ \left(\omega_n - \frac{1}{\omega_n} \right) \end{aligned} \quad \text{(B.10)}$$

Next:

$$\begin{aligned}\frac{Z_1}{Z''_m} &= \frac{j\omega_s L_{R2}}{j\omega_s L''_m} + \frac{1}{j\omega_s C_{R2}} \frac{1}{j\omega_s L''_m} = \frac{L_{R2}}{L''_m} + \frac{1}{j^2 \omega_s^2 C_{R2} L''_m} = \\ &= \frac{1}{k} - \frac{1}{\omega_n^2 \frac{1}{L_{R2} C_{R2}} C_{R2} k L_{R2}} = \frac{1}{k} - \frac{1}{\omega_n^2 k}\end{aligned}\quad (\text{B.11})$$

And finally:

$$\begin{aligned}\frac{Z_2}{R''_o} &= \frac{j\omega_s L''_{R1} + \frac{1}{j\omega_s C''_{R1}}}{R''_o} = \frac{j\omega_s L''_{R1}}{R''_o} + \frac{1}{j\omega_s C''_{R1} R''_o} = \\ &= j\omega_n \frac{1}{\sqrt{L_{R2} C_{R2}}} \frac{L''_{R1}}{R''_o} + \frac{1}{j\omega_n \frac{1}{\sqrt{L_{R2} C_{R2}}} C''_{R1} R''_o} = \\ &= j\omega_n \frac{a L_{R2}}{\sqrt{L_{R2} C_{R2}}} \frac{1}{R''_o} + \frac{1}{j\omega_n \frac{b C_{R2}}{\sqrt{L_{R2} C_{R2}}} R''_o} = \\ &= j\omega_n a \sqrt{\frac{L_{R2}}{C_{R2}}} \frac{1}{R''_o} + \frac{1}{j\omega_n b \frac{R''_o}{\sqrt{L_{R2} C_{R2}}}} = j\omega_n a Q - \frac{jQ}{\omega_n b} = \\ &= jQ \left(a\omega_n - \frac{1}{b\omega_n} \right)\end{aligned}\quad (\text{B.12})$$

Replacing in the transfer function B.4:

$$\begin{aligned}H(j\omega_n, Q) &= \frac{1}{jQ \left(\omega_n - \frac{1}{\omega_n} \right) + \left(\frac{1}{k} - \frac{1}{\omega_n^2 k} \right) \left[jQ \left(a\omega_n - \frac{1}{b\omega_n} \right) + 1 \right] + jQ \left(a\omega_n - \frac{1}{b\omega_n} \right) + 1} = \\ &= \frac{1}{jQ \left(\omega_n - \frac{1}{\omega_n} \right) + \left(\frac{1}{k} - \frac{1}{\omega_n^2 k} \right) \left[jQ \left(a\omega_n - \frac{1}{b\omega_n} \right) \right] + \left(\frac{1}{k} - \frac{1}{\omega_n^2 k} \right) + jQ \left(a\omega_n - \frac{1}{b\omega_n} \right) + 1} = \\ &= \frac{1}{\left(\frac{1}{k} - \frac{1}{\omega_n^2 k} + 1 \right) + jQ \left(\omega_n - \frac{1}{\omega_n} \right) + jQ \left(\frac{a\omega_n}{k} - \frac{1}{kb\omega_n} - \frac{a}{k\omega_n} + \frac{1}{kb\omega_n^3} \right) + jQ \left(a\omega_n - \frac{1}{b\omega_n} \right)}\end{aligned}\quad (\text{B.13})$$

The final formula is:

$$H(j\omega_n, Q) = \frac{1}{\left(\frac{1}{k} - \frac{1}{\omega_n^2 k} + 1 \right) + j \left[Q\omega_n \left(1 + \frac{a}{k} + a \right) - \frac{Q}{\omega_n} \left(\frac{1}{kb} + \frac{a}{k} + \frac{1}{b} + 1 \right) + \frac{Q}{kb\omega_n^3} \right]}\quad (\text{B.14})$$

The module of B.14 is calculated in B.15:

$$M(j\omega_n, Q) = \left\{ \left(\frac{1}{k} - \frac{1}{\omega_n^2 k} + 1 \right)^2 + \left[Q\omega_n \left(1 + \frac{a}{k} + a \right) - \frac{Q}{\omega_n} \left(\frac{1}{kb} + \frac{a}{k} + \frac{1}{b} + 1 \right) + \frac{Q}{kb\omega_n^3} \right]^2 \right\}^{-\frac{1}{2}}\quad (\text{B.15})$$

APPENDIX B. CALCULATION GAIN FORMULA IN REVERSE MODE

Appendix C

Calculation of the Input Impedance

For the CLLC resonant converter, by referring to the model in forward mode analyzed A, the input impedance is expressed as:

$$\begin{aligned}
 Z_{in} &= Z_1 + Z_m \parallel (Z_2 + R'_o) = j\omega_s L_{R1} + \frac{1}{j\omega_s C_{R1}} + \frac{jR'_o\omega_s L_m - \omega_s^2 L'_{R2} L_m + \frac{L_m}{C'_{R2}}}{R'_o + j\omega_s L'_{R2} + \frac{1}{j\omega_s C'_{R2}} + j\omega_s L_m} = \\
 &= R'_o \left(\frac{j\omega_s L_{R1}}{R'_o} + \frac{1}{j\omega_s C_{R1} R'_o} + \frac{\frac{j\omega_s L_m}{R'_o} - \frac{\omega_s^2 L'_{R2} L_m}{R_o'^2} + \frac{L_m}{R_o'^2 C'_{R2}}}{1 + \frac{j\omega_s L'_{R2}}{R'_o} + \frac{1}{j\omega_s R'_o C'_{R2}} + j\omega_s \frac{L_m}{R'_o}} \right)
 \end{aligned} \tag{C.1}$$

Let's to analyze some elements of the equation C.1 referring to equations A.5, A.6, A.7, A.8 and A.9.

1) From A.10 is known that:

$$\frac{j\omega_s L_{R1}}{R'_o} + \frac{1}{j\omega_s C_{R1} R'_o} = jQ \left(\omega_n - \frac{1}{\omega_n} \right) \tag{C.2}$$

Then, all the others elements can be expressed as:

$$2) \quad \frac{j\omega_s L_m}{R'_o} = j\omega_n \frac{L_m}{\sqrt{L_{R1} C_{R1}}} \frac{1}{R'_o} = \frac{j\omega_n k L_{R1}}{\sqrt{L_{R1} C_{R1} R'_o}} = j\omega_n k Q \tag{C.3}$$

APPENDIX C. CALCULATION OF THE INPUT IMPEDANCE

$$3) \quad \frac{\omega_s^2 L'_{R2} L_m}{R_o'^2} = \frac{\omega_n^2}{L_{R1} C_{R1}} \frac{a L_{R1} k L_{R1}}{R_o'^2} = \omega_n^2 a k \frac{\frac{L_{R1}}{C_{R1}}}{R_o'} = \omega_n^2 a k Q^2 \quad (C.4)$$

$$4) \quad \frac{L_m}{R_o'^2 C'_{R2}} = \frac{k L_{R1}}{R_o'^2 b C_{R1}} = \frac{k}{b} Q^2 \quad (C.5)$$

$$5) \quad \frac{j \omega_s L'_{R2}}{R_o'} = \frac{j \omega_n a L_{R1}}{\sqrt{L_{R1} C_{R1}} R_o'} = j \omega_n a \frac{\sqrt{\frac{L_{R1}}{C_{R1}}}}{R_o'} = j \omega_n a Q \quad (C.6)$$

$$6): \quad \frac{1}{j \omega_s R_o' C'_{R2}} = \frac{1}{j \omega_n} \frac{\sqrt{L_{R1} C_{R1}}}{R_o' b C_{R1}} = -\frac{j}{\omega_n b} Q \quad (C.7)$$

$$7): \quad j \omega_s \frac{L_m}{R_o'} = j \omega_n \frac{1}{\sqrt{L_{R1} C_{R1}}} \frac{k L_{R1}}{R_o'} = j \omega_n k Q \quad (C.8)$$

Going to substitute in C.1 and carrying out simple steps (which have been omitted), the impedance formula has been found:

$$\begin{aligned} Z_{in} &= R_o' \left(\frac{j \omega_n^2 Q - j Q}{\omega_n} + \frac{j \omega_n k Q - \omega_n^2 a k Q^2 + \frac{k}{b} Q^2}{1 + j \omega_n a Q - \frac{j}{\omega_n b} Q + j \omega_n k Q} \right) = \\ &= R_o' \left(\frac{Q^2 - \omega_n^2 Q^2 (ab + kb + k + 1) + \omega_n^4 Q^2 (ab + kb + kab) + j Q b (\omega_n - \omega_n^3 (1 + k))}{-\omega_n^2 b + j \omega_n Q [1 - \omega_n^2 b (a + k)]} \right) \end{aligned} \quad (C.9)$$

Bibliography

- [1] *Understanding Energy Trilemma*. Accessed: 2024-02-14. URL: <https://www.ieaaustral.com/world-energy-council-world-energy-trilemma-index-2022/>.
- [2] *Energy Roadmap 2050*. Accessed: 2024-02-14. URL: <https://eur-lex.europa.eu/LexUriServ/LexUriServ.do?uri=COM:2011:0885:FIN:EN:PDF>.
- [3] *Smart Grid – the Future of Energy*. Accessed: 2024-02-14. URL: <https://www.onlogic.com/company/io-hub/smart-grid-the-future-of-energy/>.
- [4] LIU Shuguang and YE Zhenxing. “Progress and prospect of electric vehicle’s v2g technology”. In: *2019 6th International Conference on Information Science and Control Engineering (ICISCE)*. IEEE. 2019, pp. 412–416.
- [5] *Global EV Outlook 2023*. Accessed: 2024-01-18. URL: <https://iea.blob.core.windows.net/assets/dacf14d2-eabc-498a-8263-9f97fd5dc327/GEV02023.pdf>.
- [6] Sebastian Rivera et al. “Electric vehicle charging infrastructure: From grid to battery”. In: *IEEE Industrial Electronics Magazine* 15.2 (2021), pp. 37–51.
- [7] J Rahulkumar et al. “An empirical survey on wireless inductive power pad and resonant magnetic field coupling for in-motion EV charging system”. In: *IEEE Access* 11 (2022), pp. 4660–4693.
- [8] *EV Battery Swapping Solution Companies in India*. Accessed: 2024-02-14. URL: <https://e-vehicleinfo.com/ev-battery-swapping-stations/>.
- [9] Sebastian Rivera et al. “Charging infrastructure and grid integration for electromobility”. In: *Proceedings of the IEEE* 111.4 (2022), pp. 371–396.
- [10] Lais Farias Martins, David Stone, and Martin Foster. “Modelling of phase-shift modulated bidirectional CLLC resonant converter”. In: *IET Power Electronics* 13.12 (2020), pp. 2628–2637.
- [11] Xiaoqiang Li et al. “Unified modeling, analysis, and design of isolated bidirectional CLLC resonant DC–DC converters”. In: *IEEE Journal of Emerging and Selected Topics in Power Electronics* 10.2 (2022), pp. 2305–2318.

BIBLIOGRAPHY

- [12] Ning Chen et al. “Synchronous rectification based on resonant inductor voltage for CLLC bidirectional converter”. In: *IEEE Transactions on Power Electronics* 37.1 (2021), pp. 547–561.
- [13] Arun Sankar, Ayan Mallik, and Alireza Khaligh. “Extended harmonics based phase tracking for synchronous rectification in CLLC converters”. In: *IEEE Transactions on Industrial Electronics* 66.8 (2018), pp. 6592–6603.
- [14] Yih-Her Yan, Yong-Nong Chang, and Zhi-Xuan Peng. “Design of a bidirectional CL3C full-bridge resonant converter for battery energy storage systems”. In: *Energies* 15.2 (2022), p. 412.
- [15] Jee-Hoon Jung et al. “Design methodology of bidirectional CLLC resonant converter for high-frequency isolation of DC distribution systems”. In: *IEEE Transactions on Power Electronics* 28.4 (2012), pp. 1741–1755.
- [16] Kai Zhou et al. “Research on dual-output port on-board charging system based on CLLC resonant converter”. In: *Plos one* 18.2 (2023), e0279558.